# The aerodynamic design of multi-element high-lift systems for transport airplanes

## C.P. van Dam*

*Department of Mechanical and Aeronautical Engineering, University of California, Davis, One Shields Avenue, Davis, CA 95616-5294, USA*

### Abstract

High-lift systems have a major influence on the sizing, economics, and safety of most transport airplane configurations. The combination of complexity in flow physics, geometry, and system support and actuation has historically led to a lengthy and experiment intensive development process. However, during the recent past engineering design has changed significantly as a result of rapid developments in computational hardware and software. In aerodynamic design, computational methods are slowly superseding empirical methods and design engineers are spending more and more time applying computational tools instead of conducting physical experiments to design and analyze aircraft including their high-lift systems. The purpose of this paper is to review recent developments in aerodynamic design and analysis methods for multi-element high-lift systems on transport airplanes. Attention is also paid to the associated mechanical and cost problems since a multi-element high-lift system must be as simple and economical as possible while meeting the required aerodynamic performance levels. © 2002 Elsevier Science Ltd. All rights reserved.

## Contents

*Tel.: +1-530-752-7741; fax: +1-530-752-4158.
*E-mail address:* cpvandam@ucdavis.edu (C.P. van Dam).

**Nomenclature**

| | |
|---|---|
| $A$ | aspect ratio |
| $a_0$ | speed of sound at standard sealevel conditions |
| $b$ | wing span |
| $C_D$ | drag coefficient |
| $C_{D_0}$ | zero-lift drag coefficient |
| $C_L$ | lift coefficient |
| $C_{L_{max}}$ | maximum lift coefficient |
| $C_{L_0}$ | lift coefficient at zero angle of attack |
| $C_p$ | pressure coefficient |
| $C_d, c_d$ | sectional drag coefficient |
| $C_l, c_l$ | sectional lift coefficient |
| $c_t$ | thrust specific fuel consumption |
| $D$ | drag |
| $e$ | Oswald efficiency factor |
| $K$ | relaminarization parameter |
| $M_\infty$ | freestream Mach number |
| $L$ | lift |
| $R$ | range |
| $\bar{R}$ | attachment line Reynolds number |
| $Re$ | Reynolds number |
| $S$ | reference wing area |
| $T$ | thrust |
| $U$ | local velocity at edge of boundary layer |
| $V_\infty$ | freestream velocity |
| $V_A$ | approach speed |
| $V_{LOF}$ | liftoff speed |
| $V_{MC}$ | minimum control speed |
| $V_{MU}$ | minimum unstick speed |
| $V_R$ | rotation speed |
| $V_{S_{min}}$ | minimum stalling speed |
| $V_{S_{1g}}$ | stall speed in steady level flight |
| $V_2$ | takeoff climb speed |
| $W$ | weight |
| $\delta_f$ | flap setting |
| $\Lambda$ | sweep angle |
| $\alpha$ | angle of attack |
| $\gamma$ | flight path angle, or intermittency |
| $\eta$ | nondimensional semi-span station, $y/(b/z)$ |
| $\theta$ | ratio of ambient temperature and temperature at standard sealevel conditions |
| $\rho$ | fluid density |
| $\upsilon$ | kinematic viscosity, $\mu/\rho$ |
| $\mu$ | absolute viscosity |

*Subscripts*

| | |
|---|---|
| e | end |
| i | initial |

| | |
|---|---|
| max | maximum |
| $\infty$ | undisturbed flow |

*Acronyms*

| | |
|---|---|
| AEO | all engines operating |
| AIAA | American Institute of Aeronautics and Astronautics |
| AGARD | Advisory Group for Aerospace Research & Development |
| ARC | Aeronautical Research Council (UK) |
| CF | cross-flow |
| CFD | computational fluid dynamics |
| DERA | Defence Evaluation and Research Agency (UK) |
| DLR | Deutsche Luft- und Raumfahrtforschung |
| DNW | Duits Nederlandse Wind tunnel |
| EET | energy efficient transport |
| ETW | European Transonic Wind tunnel |
| GD | landing gear down |
| GU | landing gear up |
| ICAS | International Council of Aeronautical Sciences |
| IGE | in ground effect |
| LLF | Large Low-speed Facility |
| LTPT | Low-Turbulence Pressure Tunnel |
| NACA | National Advisory Committee on Aeronautics (USA) |
| NASA | National Aeronautics and Space Administration (USA) |
| NFAC | National Full-Scale Aerodynamics Complex |
| NHLP | National High Lift Program (UK) |
| NLR | Nationaal Lucht- en Ruimtevaartlaboratorium (the Netherlands) |
| NTF | National Transonic Facility |
| OEI | one engine inoperative |
| OEW | operating empty weight |
| OGE | out of ground effect |
| ONERA | Office National d'Etudes et de Recherches Aérospatiales (France) |
| PDR | pressure difference rule |
| RAE | Royal Aircraft Establishment (UK) |
| RANS | Reynolds-averaged Navier–Stokes |
| RTO | NATO Research & Technology Organization |
| SAE | Society of Automotive Engineers (USA) |
| TO | takeoff |
| TS | Tollmien-Schlichting |
| TSRV | transport system research vehicle |
| WBL | wing butt line |

# 1. Introduction

The design of multi-element high-lift systems for aircraft has become increasingly important. Where early attention was mostly focused on maximum lift requirements to satisfy the high cruise wing loading needs of jet transport aircraft while retaining acceptable takeoff and landing distances, more recently the attention has turned

to reducing the complexity and weight of the high-lift systems for given maximum lift levels. Multi-element high-lift systems have a significant impact on the cost of a typical jet transport because (i) they are time consuming to design and test, (ii) their flows, geometry, and actuation and support systems are complex, (iii) they are heavy, (iv) have a high part count, and (v) are maintenance intensive. According to Rudolph [1], an aircraft's high-lift system accounts for somewhere between 6% and 11% (potentially higher for more complex configurations) of the production cost of a typical jet transport. Another example on the importance of high-lift systems for a generic large twin engine transport is presented by Meredith [2]:

1. An increase in maximum lift coefficient of 1.0% translates into an increase in payload of 22 passengers or 4400 lb for a fixed approach speed on landing.
2. An improvement in lift-to-drag ratio of 1.0% during takeoff translates into an increase in payload of 14 passengers or 2800 lb for a given range.
3. A shift of $\Delta C_L = 0.10$ of the lift curve in the linear range results in a $1°$ reduction in attitude for a given glideslope angle. This allows a reduction in required landing gear height of 14 in. for a given tail strike attitude angle and a decrease in OEW of 1400 lb.

This example demonstrates that relatively small changes in the aerodynamic performance of the high-lift system can produce large payoffs in airplane weight and performance. This sensitivity of airplane weight and performance to small changes in high-lift aerodynamics in combination with the large impact of high-lift systems on airplane cost explains why high-lift systems and their aerodynamic characteristics remain in the forefront of aerospace research.

Fig. 1 illustrates the typical effect of a multi-element high-lift system on lift. A leading-edge device such as a slat, increases the stall angle of attack, whereas a trailing-edge device such as a single-slotted Fowler flap, produces an upward shift in the lift curve. The aerodynamic performance of multi-element wings is very sensitive to
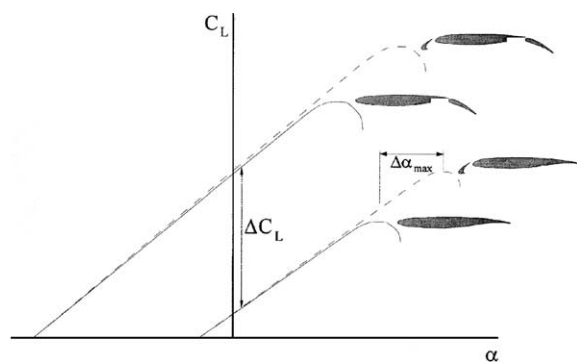


Fig. 1. Typical high-lift system and its effect on airplane lift.

small variations in the gap size and the overlap between the various elements. This in combination with the fact that the system has to perform well for a wide range of flap settings (light takeoff, heavy takeoff, landing) and the large aerodynamic loads generated by the various elements makes the support and actuation of the high-lift elements quite complicated. Fig. 2 gives an example of the resulting complexity by showing the outboard wing section of the B737-NG consisting of a slat, main element and double-slotted Fowler flap. The slat is actuated by a rack and pinion drive whereas the flaps are supported by a curved track and actuated by a screw drive linked to a rotating shaft by a gearbox.

Although high-lift systems are complex and costly, they are a necessity in order to allow airplanes to takeoff and land on runways of acceptable length without penalizing the cruise efficiency significantly as discussed in the following section. Next, the major design objectives and constraints will be discussed followed by a brief review of the flow physics of multi-element wings. No paper on high-lift aerodynamics is complete without an overview of existing high-lift systems on civil transport airplanes. The experimental and computational techniques that are being used to explore and enhance the performance characteristics of high-lift systems are discussed in the remainder of this paper, followed by an overview of several design examples.

## 2. Why high-lift systems are needed

Let us consider the range performance of a civil jet-propelled transport airplane, Airplane A, which is governed by the following well known expression:

$$R = \frac{a_0\sqrt{\theta}}{c_t} M_\infty \frac{L}{D} \ln \frac{W_i}{W_e}.$$

Airplane A has a cruise Mach number $M_\infty = 0.80$ and a lift coefficient $C_L = \sqrt{C_{D_0}\pi Ae} = 0.52$ for optimal $M_\infty L/D = 14.4$. It has an initial cruise altitude of 30,000 ft and a wing loading $(W/S)_i \approx (W/S)_{TO}$ of 147 lb/ft². On approach for landing it operates at a typical speed $V_A = 145$ knots and a maximum landing wing loading of 110 lb/ft²; 75% of $(W/S)_{TO}$. As a result, the lift coefficient on approach for landing is $C_{L_A} = 1.55$ and this translates into a $C_{L_{max}} = 1.23^2 C_{L_A} = 2.34$. (The factor 1.23 is governed by the airworthiness requirements and is explained in the next section.) This maximum lift coefficient is well beyond the capabilities of an airplane with a simple swept wing. Maximum lift coefficients for airplanes without any high-lift devices typically do not exceed 1.2. This example demonstrates the need for high-lift devices on jet-propelled civil transport airplanes such as Airplane A.

This brings up the question what the penalty in cruise efficiency would be if no high-lift system would be
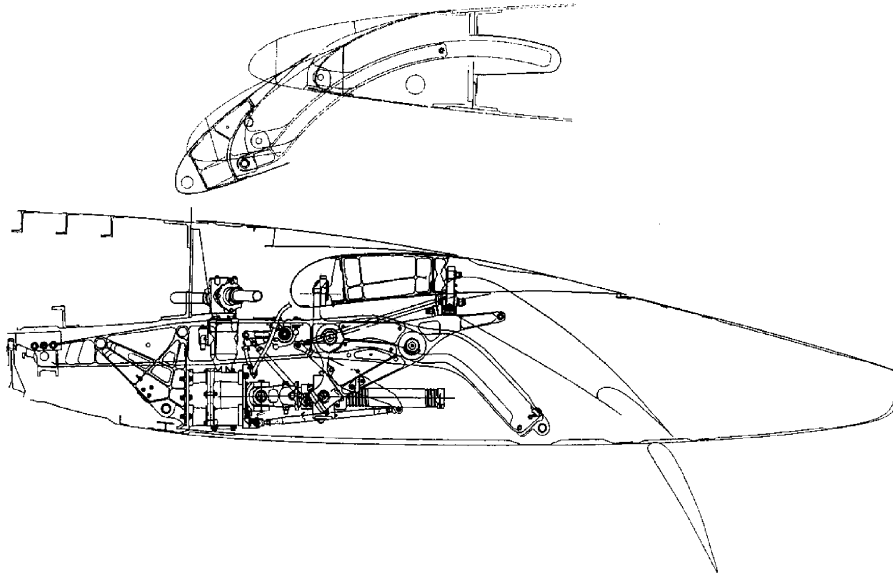
Fig. 2. Outboard wing cross section of B737-NG [129].

incorporated but instead a larger single-element wing would be adopted. We call this Airplane B and assume it has a maximum lift coefficient of 1.2 and, consequently, the maximum lift coefficient on approach for landing $C_{L_A} = C_{L_{max}}/1.23^2 = 0.79$. Given the exact same approach speed $V_A = 145$ knots, a maximum wing loading on landing of $56 \, lb/ft^2$ is calculated for Airplane B. Using the same ratio between landing and takeoff wing loading as before, we calculate a $(W/S)_i \approx (W/S)_{TO}$ of $75 \, lb/ft^2$ and cruise lift coefficient of 0.27 at $M_\infty = 0.80$ and an initial cruise altitude of 30,000 ft. Assuming that Airplane A and Airplane B have the identical drag characteristics, we calculate an $M_\infty L/D = 11.8$; 18.3% lower than that of Airplane A. Clearly an increase in cruise altitude will reduce but not eliminate this penalty. The only way for Airplane B with its large single-element wing to become competitive with Airplane A in terms of cruise efficiency is by implementing laminar flow technology. This will not only increase $L/D$ but also reduce the lift coefficient for maximum $L/D$.

Given the fact that the current generation of civil transport airplanes has mostly turbulent wings and the general lack of interest in laminar flow technology for this category of airplanes, high-lift systems will remain a necessity for the foreseeable future.

## 3. High-lift design objectives and constraints

The takeoff and landing performance of subsonic civil transport airplanes are governed by the requirements such as those listed in the Federal Airworthiness Regulations (FAR) Part 25. Figs. 3 and 4 illustrate the
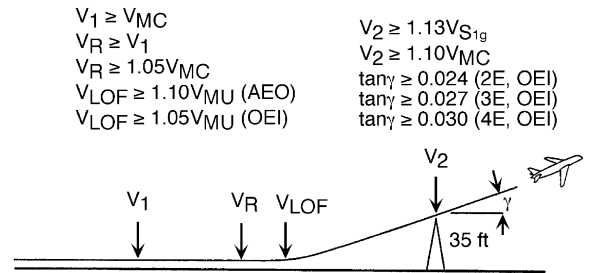


Fig. 3. Takeoff procedure for civil jet-propelled transport airplanes.
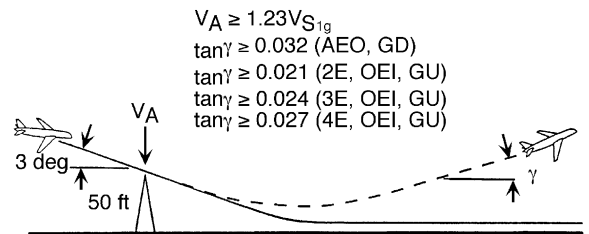


Fig. 4. Landing procedure for civil transport airplanes.

takeoff and landing maneuvers for civil transport airplanes. As explained by Ruijgrok [3], during the takeoff run the airplane at maximum takeoff weight accelerates from standstill to the rotation speed $V_R$ and from $V_R$ to the liftoff speed $V_{LOF}$. When reaching the rotation speed the pilot rotates the airplane to the desired pitch attitude angle. The rotation speed strongly

influences the takeoff distance. If $V_R$ is selected too low the takeoff run is extended because of the excessive aerodynamic drag created by the airframe in the nose high attitude during the takeoff roll. If $V_R$ is selected too high the takeoff distance is extended because of the excessive airspeed (airspeed in excess of the legal minimum) during the takeoff maneuver. At $V_{LOF}$ the lift force exceeds the weight and the airplane becomes airborne. According to the airworthiness requirements, $V_{LOF}$ must be at least 1.1 (1.05 with one engine out) times the minimum liftoff or unstick speed $V_{MU}$, where $V_{MU}$ represents the minimum airspeed at which the airplane can safely liftoff with the critical engine inoperative. Note that especially for large civil transport airplanes the rotation angle and, consequently $V_{MU}$, may be governed by the tail-scrape angle and not by the maximum lift capabilities of the airplane. The next important airspeed is the takeoff climb speed $V_2$, which must be reached at 35 ft above the ground; the end of the first-segment climb. This airspeed must be at least 1.13 times the stall speed $V_{S_{1g}}$ and at least 1.1 times the minimum control speed $V_{MC}$, where $V_{S_{1g}}$ represents the stall speed in steady level flight. Typically $V_{S_{1g}}$ is approximately 1.06 times the minimum stalling speed during slow decelerating (1 knot/s) flight, $V_{S_{min}}$ [4]. Next the airplane enters the second-segment climb. During this portion of the flight with the landing gear retracted, OGE, and the flaps still in the takeoff position, the airworthiness requirements stipulate that two-engine airplanes with one engine out have a minimum climb gradient of 0.024 (0.027 for airplanes with three engines and 0.030 for four-engine airplanes) at airspeeds greater or equal than $V_2$. The climb gradient is dependent on the thrust-to-weight ratio as well as the lift-to-drag ratio:

$$\tan \gamma \cong \frac{T}{W} - \frac{1}{L/D}.$$

Higher flap settings generally decrease $V_{S_{1g}}$ and $V_{MU}$ thereby reducing the ground-roll distance but also decrease $L/D$ thereby reducing the climb performance. Thus the aerodynamic design of the takeoff configuration involves a compromise between lift and drag [4]. Figs. 5 and 6 illustrate this compromise for an older generation jet-propelled transport airplane with higher flap settings resulting in increased $C_{L_0}$ and $C_{L_{max}}$ but also a significant drop in $L/D$. The lift and drag results shown in these two figures were obtained in flight and corrected for thrust and acceleration effects. Typical data runs were terminated at a lift coefficient just shy of the stall angle of attack. Based on the lift curves in Fig. 5 and assuming that the highest lift coefficients in this figure represent the maximum lift coefficients for the different flap settings, the takeoff lift coefficients were determined by dividing the maximum lift coefficients by $1.13^2$ for $\delta_f = 5°$ and $15°$.
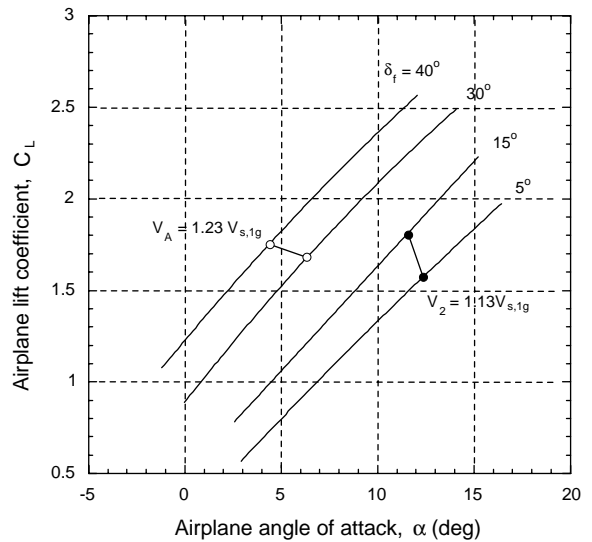


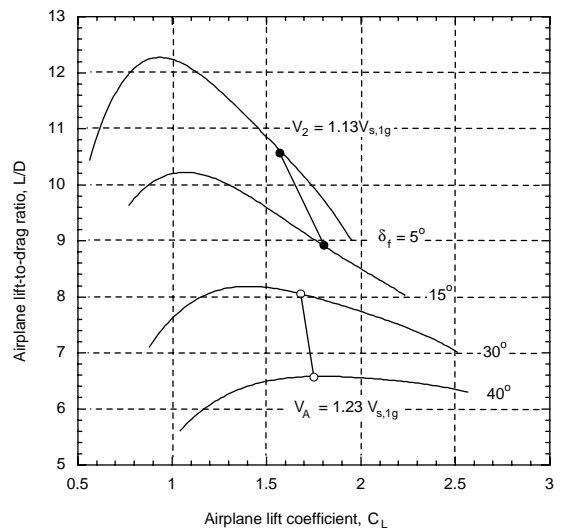Fig. 5. Lift curves for a typical civil transport airplane.



Fig. 6. Lift-to-drag ratios for a typical civil transport airplane.

Fig. 4 illustrates the landing maneuver for civil transport airplanes. On final approach for landing the airplane at maximum design landing weight descends at a glidepath angle of $3°$. At 50 ft above the ground the airworthiness requirements stipulate that the airplane has an airspeed, $V_A$, of at least 1.23 times $V_{S_{1g}}$ (or 1.3 times $V_{S_{min}}$) where $V_{S_{1g}}$ is now the stall speed for the airplane in the landing configuration. In Figs. 5 and 6 the corresponding lift conditions are determined by dividing the maximum lift coefficients by $1.23^2$ for $\delta_f = 30°$ and $40°$. Note that the approach angle of attack may be governed by the pilot's visibility and not by the

maximum lift capabilities of the airplane. Climb performance requirements and, thus airplane lift-to-drag ratio, play also a role during the approach and landing portions of the flight. The climb gradient (with all engines operating, landing gear down, and airspeed at 1.23 times $V_{S_{1g}}$) must be at least 0.032 at a thrust level corresponding to that obtained 8 s after moving the throttles from minimum flight idle to maximum takeoff position. In addition there is the climb gradient requirement for the airplane in the approach configuration with the critical engine inoperative (climb gradient at least 0.021 for two-engine airplanes, 0.024 for three-engine airplanes, and 0.027 for four-engine airplanes). These last two requirements are the so-called go-around or balked landing requirements.

In conclusion the aerodynamic design of the high-lift system requires a careful tradeoff between maximum lift capabilities, lift-to-drag ratio, and lift capabilities at the tail-scrape angle on takeoff and at the approach angle on landing.

## 4. Flow physics of multi-element high-lift systems

The problem of high-lift aerodynamics has been studied since the early years of aviation but in the early 1950s, after nearly 40 years of research, the body of knowledge was still somewhat limited and was compiled in about four publications [5]: (i) NACA TR 824 by Abbott, von Doenhoff, and Stivers [6], (ii) *Theory of Wing Sections* by Abbott and von Doenhoff [7], (iii) NACA TR 938 by Cahill [8] and, (iv) ARC R&M 2622 by A.D. Young [9]. It was not until the early 1970s that significant progress was made in formulating a theoretical basis for high-lift aerodynamics as a result of the insight into the underlying aerodynamic principles provided by A.M.O. Smith. Smith [10,11] laid out the five predominant favorable effects of gaps (or slots) in multi-element airfoil flows. The circulation of a forward element induces flow on a trailing element counter to the natural acceleration around the leading edge. This so-called *slat effect* reduces the leading-edge suction peak on the trailing element, thus reducing pressure recovery demands and delaying separation. The trailing element, however, induces a *circulation effect* on the forward element which tends to increase the loading on the forward element, increasing the lift, but also increasing pressure recovery demands. Yet, the high velocity flow on the upper surface of the trailing element allows the flow to leave the forward element at a higher speed. This *dumping effect* reduces the pressure recovery of the forward element and favors *off-surface pressure recovery*, which is more efficient than recovery in contact with a wall. Finally, each element has a *fresh boundary layer* which originates on that element. A thin, turbulent boundary layer can withstand stronger pressure gradi-

ents than a thick one and is less likely to separate. Effectively, the overall pressure recovery of the multi-element system is divided among all the elements, but the boundary layer does not continuously grow along the chord as it would if the system was a single element.

The primary viscous effect of gaps is the existence of individual wakes from each element of the system. These wakes are thought to provide a damping effect on the pressure peak of trailing elements, reducing the tendency of the flow to separate. Yet, the wakes often tend to merge with the boundary layer of the trailing element. The resulting confluent boundary layer is much thicker than an ordinary boundary layer, so the likelihood of separation increases. Clearly, optimizing the gap size requires a balance between the inviscid and viscous effects which favor smaller and larger gaps, respectively.

The correct scaling and simulation of boundary-layer flows over three-dimensional swept wings in the high-lift configuration is strongly dependent on the type and location of transition [12]. There are generally five types of flow mechanisms that can trigger transition: Tollmien-Schlichting (TS) and inflectional instability, laminar separation, crossflow (CF) instability, attachment-line instability, and contamination by turbulent shear layers emanating from upstream elements. Note, of these transition mechanisms, only the ones governed by TS and inflectional instability, laminar separation, and turbulence contamination are relevant in two-dimensional high-lift flows. In particular, the flow along the attachment line (i.e., the location along the leading edge where the component of the freestream normal to the leading edge stagnates but the tangential component, $V_\infty \sin \Lambda$, remains) can be a significant factor in the assessment and scaling of three-dimensional high-lift system aerodynamics as first pointed out by Woodward et al. [13]. The attachment-line boundary layer can be laminar, transitional, or turbulent, depending on the pressure distribution, the leading-edge sweep angle, the Reynolds number, and surface roughness and flow contamination. If attachment-line transition occurs, the resulting changes in the development of boundary layer flows can significantly influence the downstream turbulent flow field (i.e., confluent boundary layers and onset of separation). Relaminarization of the flow downstream of a turbulent attachment line can occur if the streamwise flow acceleration is sufficiently strong. If the flow ahead of a steep adverse pressure gradient along the upper surface of the elements is laminar, an additional Reynolds-number effect can occur due to the presence of a laminar-separation bubble and its effect on subsequent turbulent-flow behavior.

The issues of leading-edge transition and relaminarization are important in the extrapolation of sub-scale, three-dimensional, wind-tunnel results to full-scale flight conditions. Typically, the wind-tunnel data used to extrapolate maximum lift to flight conditions are

obtained at Reynolds numbers where wing stall is dominated by conventional scale effects [13]. Conventional scale effects refer to the increase of maximum lift with Reynolds number due to the thinning of the turbulent boundary layer in the wing trailing edge region and the subsequent aft shift of the trailing-edge flow separation point. At higher flight Reynolds numbers, attachment-line transition can occur, causing turbulent flow to start from the attachment line. By shifting the starting point of the turbulent boundary layer forward, the trailing-edge separation location can also shift forward due to the increased growth of the turbulent boundary layer. Because of the increased extent of trailing-edge separation, a significant reduction in maximum lift may occur. However, because of steep favorable pressure gradients associated with high-lift flows, relaminarization is also possible for some sections of the wing and would alleviate some of the lift loss due to attachment-line transition. In a high-Reynolds-number wind-tunnel investigation of a swept-wing configuration without slats, maximum-lift losses of the order of 15 percent have been measured when transition occurred along the attachment line and relaminarization did not occur [2]. For multi-element sections, there is also the effect of increased effective flap gap due to the thinning of the boundary layers at higher Reynolds numbers.

An important parameter when studying the transition characteristics of the attachment-line boundary layer is the attachment-line Reynolds number, $\bar{R} = W_\infty \kappa / \nu$, where $W_\infty = V_\infty \sin \Lambda$ is the spanwise component of the freestream velocity, and $\kappa = (\nu / U_n')^{0.5}$ is the characteristic length. The quantity, $U_n'$, represents the inviscid velocity gradient at the attachment line in the direction normal to it. Gaster [14], Pfenninger [15], and Poll [16] provide additional information on the attachment-line Reynolds number. Their studies, among others, have shown that for $\bar{R} < 245$, the attachment-line boundary layer will tend to remain laminar, and turbulent contamination introduced in the boundary layer by significant surface roughness and intersecting turbulent shear layers decays. For $\bar{R} > 245$, the turbulence self-sustains, causing the attachment-line flow, as well as the flow downstream of the attachment line, to become turbulent. In the absence of any contamination, the attachment line remains laminar, and viscous instability followed by rapid transition occurs only if $\bar{R} > 580$ [17].

A convenient parameter often used to characterize the reversion from turbulent to laminar flow is the inverse Reynolds number, $K = (U \zeta / \nu)^{-1}$, where the characteristic velocity is represented by the local inviscid velocity $U$, and $\zeta = U / U_s'$ represents the characteristic length. Here $U_s'$ denotes the velocity gradient along the inviscid streamline. Launder and Jones [18] and Narashimha and Sreenivasan [19] provide additional information on the

relaminarization parameter, $K$. In two-dimensional flows, relaminarization is shown to occur for values of $K$ in excess of approximately $3 \times 10^{-6}$. Little data are available for three-dimensional wing flows; however, Beasley [20], Hardy [21], Arnal and Juillen [22], and Meredith [2] suggest that a value of $K$ in excess of $3 \times 10^{-6}$ may also indicate relaminarization in three-dimensional wing flows if $K$ is evaluated along the inviscid surface streamline.

Flight experiments on NASA Langley's TSRV (B737-100) airplane were conducted to document flow characteristics for further understanding of high-lift flows [23–27]. The results of these flight experiments provide a good example of the complexity of the flow about three-dimensional multi-element high-lift systems and the diversity of the transitional mechanisms. For the slat near WBL 324 (Fig. 7) and the airplane in the flaps-15 configuration, the boundary-layer state observations are summarized in Fig. 8. Starting at low angles of attack, the attachment line resides on the upper surface and, consequently, the suction peak occurs on the lower surface. This causes rapid growth of TS instabilities followed by transition on the backside of the suction peak. The attachment line is laminar at this point as demonstrated by the open circular symbols at and just downstream of the attachment line on the upper surface of the slat. In the favorable pressure gradient flow along the upper surface, rapid growth of CF instabilities causes transition ahead of the trailing edge at these low angle-of-attack conditions. With increasing angle of attack, the lower-surface suction peak diminishes resulting in less TS growth and, consequently, an aft movement of the transition location. At an angle of attack of approximately $3.5°$ the lower surface, until the slat heel, is completely laminar. With increasing angle of attack, the upper-surface region experiencing a favorable pressure gradient becomes shorter resulting in less CF growth and, consequently, an aft movement of the
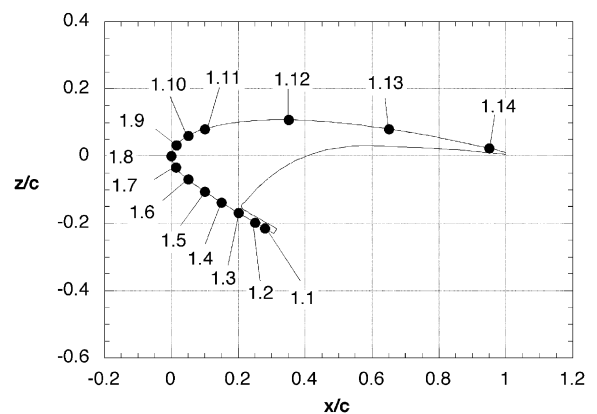


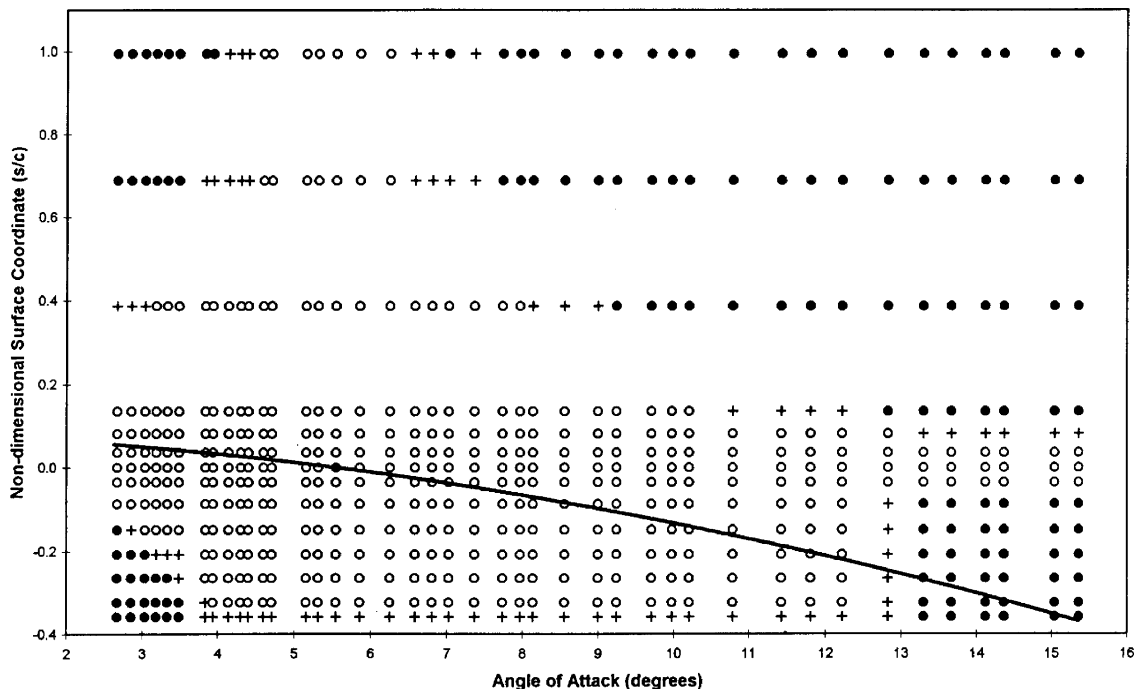Fig. 7. Cross-sectional view of slat with hot-film locations.

Fig. 8. Summary of observed boundary-layer state changes on slat near WBL 324 (60 percent semi-span station) and the airplane in the 15° flap configuration and steady flight at pressure altitude of 5000 ft: ●, turbulent; ○, laminar; +, transitional; —, attachment-line location. Note: angle of attack is that of the airplane.

transition point. Beyond an angle of attack of approximately 5°, the leading-edge suction peak develops on the upper surface and rapid growth of TS instabilities on the backside of the suction peak leads to a forward movement of the transition location on the upper surface. On the lower surface, the flow remains laminar until an angle of attack of approximately 13°, the onset of attachment-line transition. Correlation of the hot-film results and the calculated attachment-line Reynolds numbers indicates that the onset of attachment-line transition occurs at $\bar{R}$ of about 340; significantly above the $\bar{R} = 245$ level for large disturbances. The fact that attachment-line transition occurred at $\bar{R}$ lower than the instability limit of 580 indicates that there likely was an effect of residual roughness or spanwise discontinuities in the slat geometry. Note the fact that even at very high angles of attack, a region near the leading edge of the slat remains laminar although the attachment line is turbulent at those conditions. Correlation of the hot-film results and the calculated relaminarization parameter indicates that the relaminarization parameter, $K$, exceeds $3 \times 10^{-6}$ by a large margin, and the flow is shown to reverse to a laminar state in the slat leading-edge region. On the upper surface, the flow retransitions to the turbulent state under the influence of the adverse pressure gradient downstream of the leading-edge suction peak.

The experimental data presented and discussed in [23,24] show that extended regions of laminar flow occur on multi-element wings at high-lift conditions. On the B737-100, the entire slat (except for the cove) experienced laminar flow over a wide angle-of-attack range for all flap settings. In the landing configuration ($\delta_f > 25°$), the leading-edge region of the main element was laminar at medium-to-high-lift conditions. The fore flap was typically laminar over at least the initial 40 percent of the upper surface and the initial 5 percent of the lower surface. The fact that extended regions of laminar flow on high-lift systems are achievable and maintainable (at least for this class of transport airplanes) coupled with the sensitivity of high-lift aerodynamic performance to transition location has significant implications in terms of the requirements that should be put on CFD simulations and wind-tunnel testing. If the goal of the modeling is to accurately predict the high-lift characteristics of the full-scale vehicle in flight, then the extent of laminar flow attained in the CFD simulations and wind-tunnel tests should match that achieved in flight.

## 5. Overview of existing high-lift systems

No paper on the aerodynamic design of multi-element high-lift systems is complete without an overview of the

Table 1
Leading-edge high-lift devices on several civil transport airplanes [1]

| Boeing | | Douglas | | Airbus | |
|---|---|---|---|---|---|
| B707-320 | 2 position slats[a,b] | DC8 | Slots | A300 | 3 position slats[a] |
| B727 | 2 position slats[a,b] | DC9-10 | None | A310 | 3 position slats[a] |
| B737 | 3 position slats[c,b] | DC9-20/30/40/50 | 2 position slats[a] | A320 | 3 position slats[a] |
| B747 | Krüger | DC10 | 3 position slats[a] | A321 | 3 position slats[a] |
| B757 | 3 position slats[c] | MD80/90 | 3 position slats[a] | A330 | 3 position slats[a] |
| B767 | 3 position slats[c] | MD11 | 2 position slats[a] | A340 | 3 position slats[a] |
| B777 | 3 position slats[a] | | | | |

[a] Without slave tracks.
[b] Inboard Krügers.
[c] With slave tracks.

systems that are being used on civil transport jets. In-depth overviews are provided by Rudolph [1] and Niu [28]. Here a brief overview is presented to familiarize the reader with the various leading- and trailing-edge devices and their actuation and support systems.

Most civil transport jets use actively controlled slats or Krüger flaps to protect the leading edge of the wing (Table 1). Earlier airplane designs such as the B727 use two-position slats but more current designs favor three-position slats with optimized positions for cruise, takeoff and landing. The landing position is almost always slotted to maximize lift but the takeoff position is sealed on some configurations and slotted on others. Fig. 9 depicts a typical deployment schedule of a three-position slat with the trailing edge of the slat sealed against the fixed leading edge for takeoff. This setup minimizes drag when compared to the slotted leading edge as indicated by Nield [29] for the B777. However, Wedderspoon [30] reports that a slotted position gave the lowest takeoff drag for the A320 in high Reynolds number wind tunnel testing. This divergence of findings is not unexpected given the reality that the optimum slat position is dependent on the configuration, Reynolds number, and Mach number. It is this dependence combined with the fact that small changes in high-lift performance can have a critical effect on airplane performance and economics that makes high-lift system design and optimization such an important and complex problem.

Krüger flaps are used on several civil transport configurations because they tend to be lighter and simpler. However, Krüger flaps usually have only two positions (cruise and extended) and, as a result, takeoff performance may be somewhat compromised in comparison to that of three-position slats. An example of this tradeoff is given by Nield [29] in his description of the high-lift system development of the B777. In Fig. 10 the drag at takeoff for a two-position Krüger is compared against that of a three-position slat for given maximum lift performance in the landing configuration.
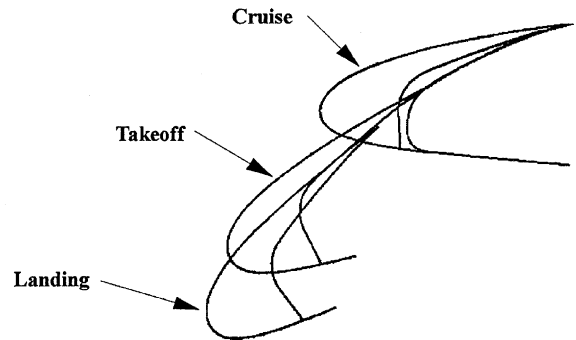


Fig. 9. Three-position slat on B777 (picture courtesy of the Boeing Company).
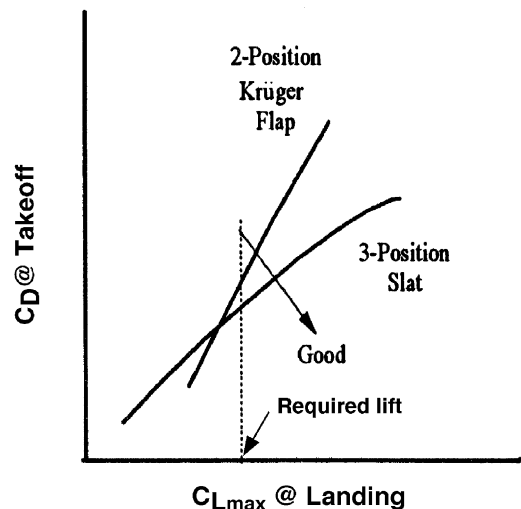


Fig. 10. Leading-edge device tradeoff study [29].

Based on this type of analysis as well as wind tunnel test data it was decided to protect the leading edge of the twin-engine B777 by slats instead of Krüger flaps. For four-engine configurations takeoff drag is less of an issue

than for twins and as a result Krüger flaps may provide the best compromise between high-lift performance, weight, and cost. This explains why the leading edge of the B747 is protected by sealed bullnose Krüger flaps (rigid panels equipped with retractable leading edge) inboard of the inboard strut and vented variable camber Krüger flaps outboard (Fig. 11). An advantage of Krüger flaps over slats is that only the pressure surface of the cruise airfoil is affected by the integration of the leading edge device, and the resulting surface steps and gaps, into the cruise wing. The lack of surface discontinuities on the suction surface has made the Krüger flap the leading-edge device of choice for laminar flow wing designs as illustrated by the study of Moens and Capbern [31].

After selecting the leading edge device and its optimum positions, the aerodynamicist tends to hand things over to the mechanical designer who is in charge of the development of the mechanism that supports and deploys the leading edge device. However, the mechanism can have a major effect on the aerodynamic performance and, maybe more importantly, on system weight and cost. For instance, to obtain a sealed slat position on takeoff a slave drive system is often required (Table 1). The slave links run in auxiliary tracks and rotate the slat in addition to the rotation provided by the slat main track [1]. This additional degree of freedom requires the slat to be pinned instead of rigidly attached to the main track. So although the sealed takeoff requirement may improve the aerodynamic performance,

it may also result in increased system complexity, weight, and cost. In the development of the B777 it was found that by making some changes to the fixed leading edge and the slat track, the slat in the takeoff position could be sealed without the addition of slave links resulting in a significant cost savings. This example illustrates the benefit of strong cooperative efforts between various disciplines early in the aircraft design stages. Several different leading-edge drive systems are being used on civil transport airplanes with rotary drives becoming the system of choice. Fig. 12 provides a good example of the slat actuation and support system used on the A330/340. The inboard slat has a separate track and drive system with rotary actuators whereas the six outboard slats use constant-radius tracks and rack and pinion drive [1].

There is quite a variation in flap configurations (Table 2) and the systems used to actuate and support these trailing edge devices (Table 3). On some older generation transport jets such as the B727 triple-slotted Fowler flap systems are used. Newer generation configurations favor single- and/or double-slotted flap systems with Fowler motion. (Fowler motion denotes the aft motion of the flaps during deployment resulting in increased planform and, hence, lift.) The decision to select one or two flap elements involves much more than just maximum lift coefficient. Insightful recent papers on this decision process have been written by Nield [29] who describes the many issues Boeing had to deal with during the design and development of the B777 and by Flaig and Hilbig [4] who describe the hurdles Airbus faced during the development of the A321.

The aerodynamic efficiency of the high-lift system is not only dependent on the number of flap elements and whether or not the flaps are continuous or are separated by a thrust gate and/or inboard aileron, the support and actuation system plays also a crucial role. Flap support systems can be divided into four categories: (i) fixed hinge, (ii) linkage, (iii) track, and (iv) hybrid systems. Fixed hinge systems are relatively simple but have a very restricted Fowler motion schedule. In order to obtain more Fowler motion the dropped hinge has to be moved further down resulting in a larger flap fairing and, hence, increased cruise drag penalty. An example of a fixed hinge mechanism is shown in Fig. 13 depicting the
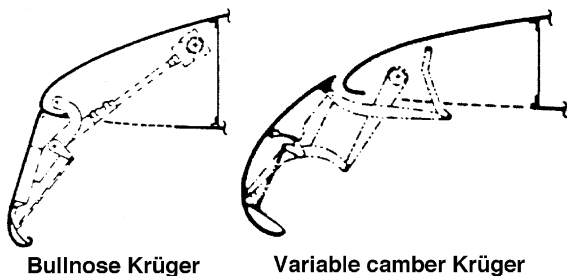


**Bullnose Krüger**          **Variable camber Krüger**

Fig. 11. Inboard bullnose Krüger and outboard variable camber Krüger on B747 [131].



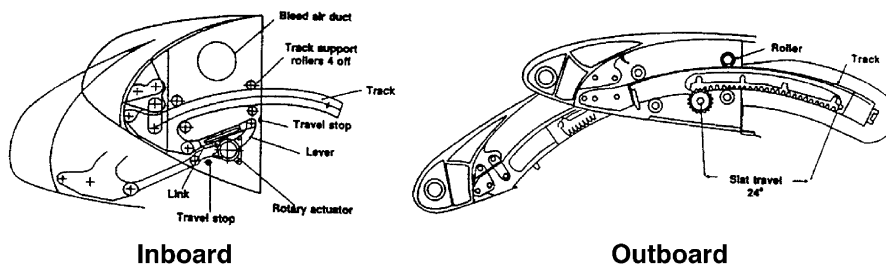**Inboard**                              **Outboard**

Fig. 12. Slat actuation and support mechanisms on A330/340 [1].

Table 2
Trailing-edge high-lift devices on several civil transport airplanes [1]

| Boeing | | Douglas | | Airbus | |
|---|---|---|---|---|---|
| B707 | Fixed vane/main double | DC8 | Fixed vane/main double | A300 | Main/aft double |
| B727 | Triple slotted | DC9 | Fixed vane/main double[a] | A300-600 | Single slotted[b] |
| B737 Classic | Triple slotted | DC10 | Articulated vane/main double | A310 | Articulated vane/main double inbd[b], single slotted outbd |
| B737 NG | Main/aft double[c] | MD80/90 | Fixed vane/main double | A320 | Single slotted |
| B747 | Triple slotted | MD11 | Articulated vane/main double | A321 | Main/aft double[c] |
| B747 SP | Single slotted | | | A330 | Single slotted[d] |
| B757 | Main/aft double[c] | | | A340 | Single slotted[d] |
| B767 | Main/aft double inbd[b], single slotted outbd | | | | |
| B777 | Main/aft double inbd[e], single slotted outbd | | | | |

[a] Double-vane/main triple-slotted inboard.
[b] Drooped inbd aileron.
[c] Single slotted thrust gate.
[d] Inbd half of aileron drooped.
[e] Drooped and slotted inbd aileron.

Table 3
Trailing-edge flap mechanisms on several civil transport airplanes [1]

| Boeing | | Douglas | | Airbus | |
|---|---|---|---|---|---|
| B707 | Internal track | DC8 | Internal four bar linkage | A300 | External hooked track |
| B727 | External hooked track | DC9 | External hinge | A310 | External hooked track |
| B737 Classic | External hooked track | MD80/90 | External hinge | A320 | Link/track mechanism with one link (aft) |
| B737 NG | External hooked track | DC10 | External hinge | A321 | Link/track mechanism with one link (aft) |
| B747 | External hooked track | MD11 | External hinge | A330 | Link/track mechanism with one link (forward) |
| B747 SP | Four bar linkage | | | A340 | Link/track mechanism with one link (forward) |
| B757 | External hooked track | | | | |
| B767 | Six bar linkage | | | | |
| B777 | Six bar linkage inbd, four bar linkage outbd | | | | |

system used to support and deploy the vane-main flaps on the DC-9/MD80/B717. Linkage systems are more complex than fixed hinge systems but provide more kinematic freedom to optimize flap positions while maintaining small flap support fairing. An example of a linkage system is shown in Fig. 14 depicting the four-bar linkage system used to support and actuate the outboard flap on the B777. Track systems involving rollers inside an 'I' beam to support the flap provide the ultimate freedom to optimize flap position for both takeoff and landing but these types of systems tend to be heavier than linkage and fixed hinge systems. An example of a track system is shown above in Fig. 2

depicting the curved track used to support the main-aft flaps on the B737 NG. Hybrid systems such as the link/track mechanism provide an interesting compromise to the flap support problem with the main advantage being improved roller/track wear characteristics [1]. An example of a link/track system is shown in Fig. 15 depicting the straight sloped track and linkage system used to support and actuate the single flap on the A320.

The summaries provided in Tables 1–3 demonstrate the wide variety of high-lift systems in use on jet-propelled civil transport aircraft. Convergence appears to be developing in terms of the types of leading edge devices (slats and Krügers) and the system used to

actuate (rotary actuator) these devices. At the trailing edge, single- and double-slotted Fowler flaps have become the high-lift devices of choice. However, significant discrepancy remains in terms of the systems used to support and actuate these flaps. These flap mechanisms play a critical role in the flap optimization process in that they provide critical kinematic constraints. In Section 10 the effects of the actuation and support system on the aerodynamic performance will be further illustrated.
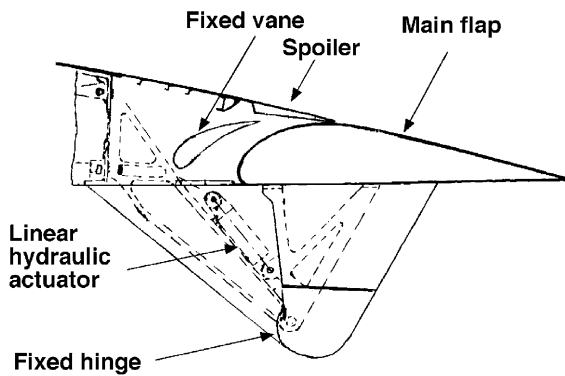


Fig. 13. Fixed hinge mechanism used to support flap on DC9/MD80/B717 [28].

## 6. Computational methods

The high-lift performance of multi-element airfoils and wings is governed by inviscid as well as viscous effects. An insightful example of the resulting tradeoff between inviscid and viscous effects is presented by Brune and McMaster [32] (based on wind-tunnel data generated by Foster et al. [33]) in their review of computational methods applied to high-lift systems. Fig. 16 depicts the lift of a two-element airfoil with a slotted trailing-edge flap at a constant angle of attack. With decreasing gap size the inviscid lift is shown to increase. However, the actual measured lift indicates an optimum gap size of approximately $0.02c$. The lift loss at larger gap sizes is mostly the result of the boundary-layer development along the main element and the flap. Whereas the lift loss at smaller gap sizes is aggravated by the confluence of the main element wake and the boundary layer along the upper surface of the flap. This multi-element lift optimization study shows the importance of both the viscous as well as inviscid flow physics and demonstrates the need for computational methods that capture both the viscous and the inviscid phenomena.

### 6.1. Two-dimensional methods

Computational methods that solve the Reynolds-averaged Navier–Stokes equations or a subset of these equations are now routinely being used in the design and



Fig. 14. Four-bar linkage system used to support and actuate outboard single-slotted flap on B777 [1].
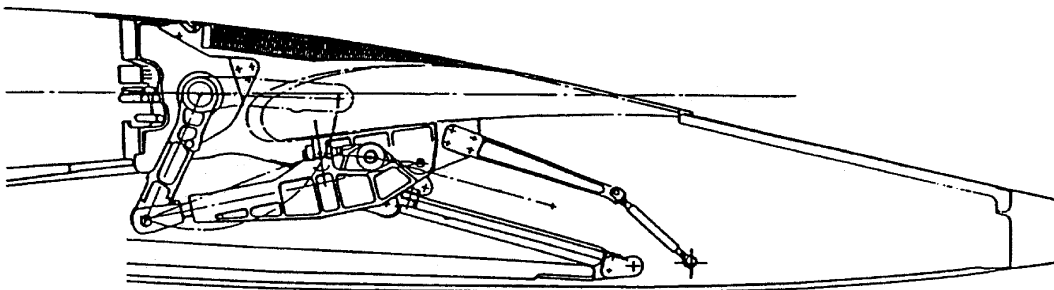


Fig. 15. Link-track mechanism used to support and actuate single-slotted flap on A320 [1].
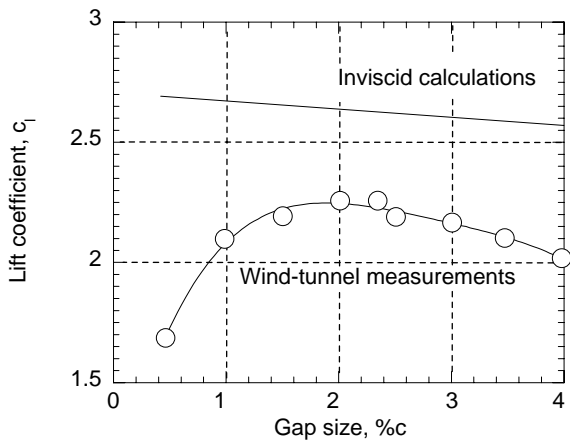
Fig. 16. Effect of flap gap on lift coefficient of a two-element airfoil at $\alpha = 0^\circ$, $Re = 3.7$ million, $M_\infty = 0.2$ [32].

analysis of multi-element airfoils. Until fairly recently, flows over multi-element airfoils were mostly analyzed with interaction methods which employ separate inviscid and viscous flow solvers coupled in an interactive manner [34]. Recent representative methods in this class are Kusunose et al. [35], Drela [36,37], Cebeci et al. [38,39], Le Balleur and Néron [40], and Arnold and Thiele [41]. All of these interaction methods provide strong coupling between the solutions of the inviscid and the viscous equations allowing for the capture of significant regions of separated flow such as in slat and main-element coves.

Probably, one of the most successful viscous/inviscid interaction methods for multi-element airfoils is the MSES code by Drela [36,37]. This method is a direct extension of the single-element viscous/inviscid methodology employed in the ISES code [42,43]. A streamline-based discretization of the Euler equations is used to compute the inviscid flow. A multi-equation integral formulation including a transition prediction algorithm is used to describe the shear layers. The viscous and inviscid regions are coupled through the displacement thickness and edge velocity, with a Newton method being used to solve the entire coupled system of equations. Figs. 17 and 18 present results for a four-element airfoil at $Re = 2.0 \times 10^6$ and $M_\infty = 0.16$. Fig. 17 depicts the streamline grid in the leading-edge region after the solution has converged at $\alpha = 6.13^\circ$. The displacement body representation used to model the shear layers clearly depicts the massive separation on the backside of the leading-edge device. Fig. 18 shows the computed lift and drag coefficients in comparison to the wind-tunnel measured results. Good agreement is obtained for most of the angle-of-attack range; however, maximum lift is overpredicted. Drela [36] attributes this discrepancy to the lack of wake-boundary layer inter-action (confluence) effects in the method.
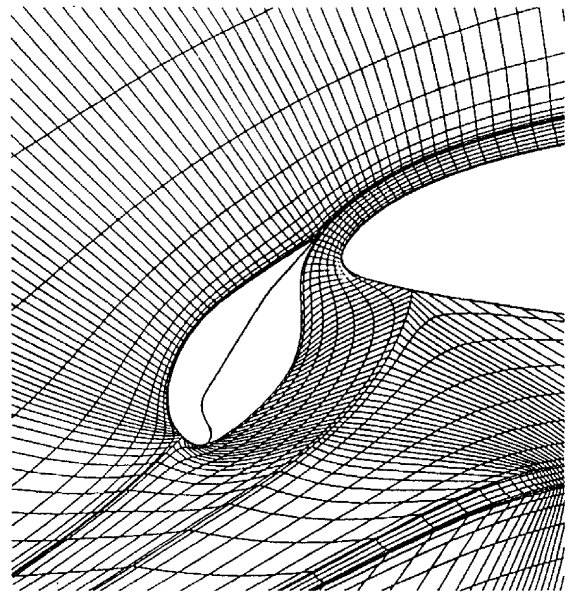


Fig. 17. Streamline grid depicting flow separation on backside of leading-edge device of four-element airfoil at $\alpha = 6.13^\circ$, $Re = 2.0 \times 10^6$ and $M_\infty = 0.16$ (Originally published in "Newton Solution of coupled viscous/inviscid multielement airfoil flows," M. Drela, AIAA Paper 90–1470, June 1990. Copyright © 1990 by the American Institute of Aeronautics and Astronamtics, Inc. Reprinted with permission.).

The method by Le Balleur and Néron [40] calculates the inviscid two-dimensional incompressible flow about multi-element airfoils using a panel method based on sources and vortices. The viscous regions layers are calculated by an integral method using a direct solution methodology when the flow is attached and an inverse methodology when flow separation is detected. The two sets of equations are coupled using a semi-inverse algorithm with relaxation that allows the analysis of fully separated flows. Thibert et al. [44], Moens and Capbern [31] and Capbern [45] applied this method, called VIS18, to design and analyze high-lift devices for general aviation and transport aircraft. Figs. 19 and 20 show representative results of these design studies and the ability of the method to handle complex configurations and separated flows. Fig. 19 depicts the computed streamlines near maximum lift. The displacement body representation used to model the shear layers clearly depicts the flow separation in the cove regions of the Krüger and main element as well as the trailing-edge region of the flap. Fig. 20 shows the computed lift curve in comparison to the wind-tunnel measured lift data. Also for this viscous/inviscid interaction method accurate predictions are obtained for most of the angle-of-attack range.

The above results and also the comparative results from a CFD challenge reported by Klausmeyer and Lin [46] demonstrate that viscous/inviscid interaction
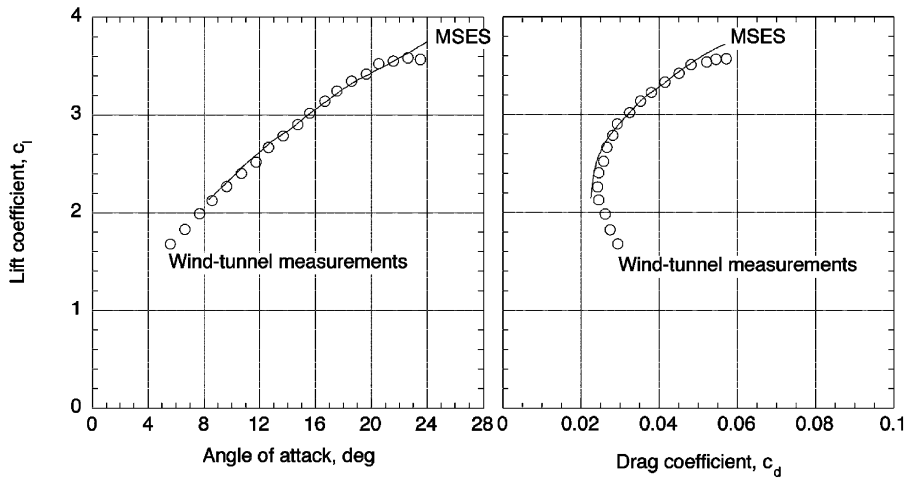
Fig. 18. Comparison of computed and experimental results for lift curve and drag polar for four-element airfoil at $Re = 2.0 \times 10^6$ and $M_\infty = 0.16$ [36].
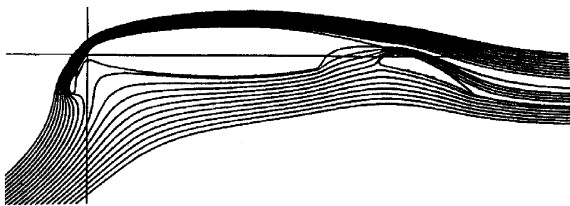


Fig. 19. Streamlines near maximum lift computed with viscous–inviscid interaction method for three-element airfoil with Krüger flap and single-slotted flap [44].
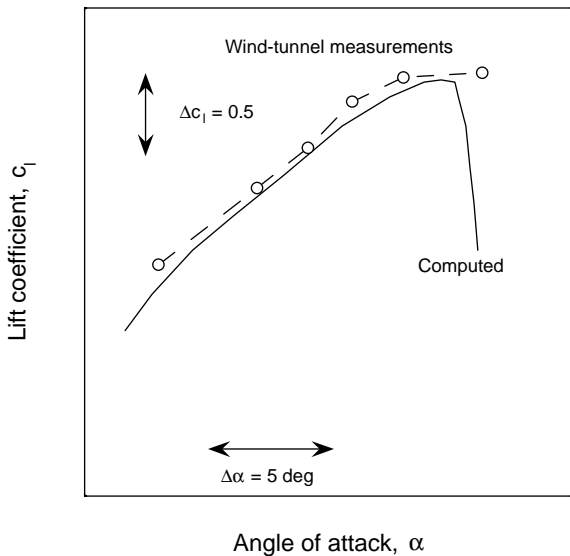


Fig. 20. Comparison of computed and experimental results for three-element airfoil with Krüger flap and single-slotted flap at $Re = 1.1 \times 10^6$ [44].

methods can provide excellent predictions and are often more accurate than methods based on the Reynolds-averaged Navier–Stokes equations. Still when it comes to solving multi-element flow problems, interaction methods have slowly fallen out of favor for several reasons. First, because of problems encountered with wakes, confluence, and massive separation, interaction methods tend to be less robust than 2D Navier–Stokes methods. Second, the extension to solve three-dimensional flow problems is more straightforward for Navier–Stokes methods than for viscous/inviscid interaction methods. A large number of Reynolds-averaged Navier–Stokes methods have been developed in the recent past. Representative methods are described by Rogers et al. [47–52] (INS2D), Shima et al. [53], Nelson et al. [54] (ARC2D), Fritz [55], Dafa'Alla and Saliveros [56] (RANSMB), and Jasper et al. [57,58] (CFL3D) for flows about multi-element airfoils on structured meshes, and Barth [59], Davis and Matus [60] (RAMPANT), Mavriplis et al. [61] (NSU2D), Anderson et al. [62,63] (FUN2D), and Dafa'Alla and Saliveros [56] (AIR-UNS2D) for flow solutions on unstructured meshes. Additional methods are discussed by Klausmeyer and Lin [46] and Lindblad and de Cock [64]. All of these methods, except INS2D, solve the compressible Reynolds-averaged Navier–Stokes equations. Also, some of these methods are limited to solving the governing equations in 2D whereas others are 3D methods that are applied to solve 2D flows over multi-element airfoils.

A good example of an unstructured grid solver is the method, FUN2D, by Anderson et al. [62,63] developed to compute the compressible viscous flow about complex geometries such as multi-element high-lift systems. Fig. 21 depicts a near view of a typical mesh for a three-element airfoil. This particularly mesh consists of 45,902 nodes and was generated using the mesh
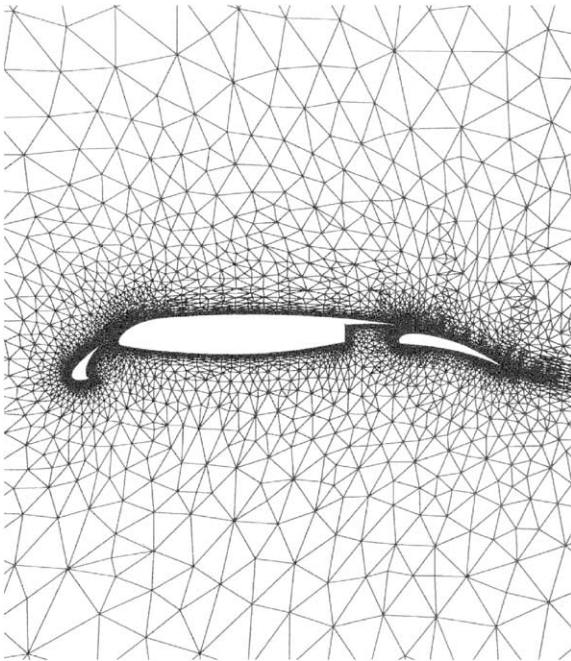
Fig. 21. Near view of unstructured mesh about three-element airfoil [62].
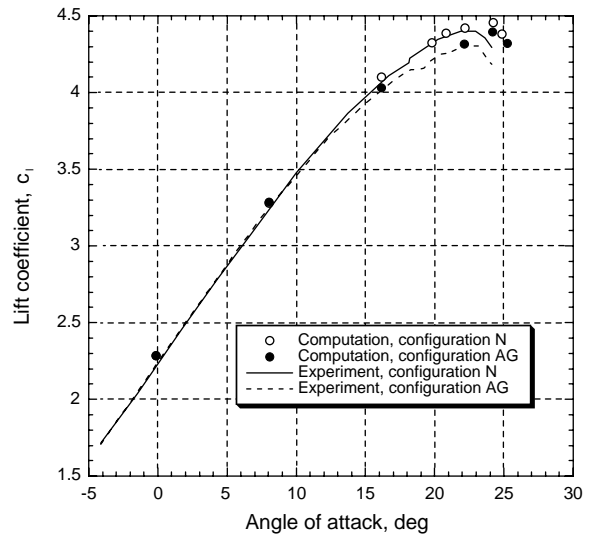


Fig. 22. Comparison of computed and experimental results for three-element airfoil in two different configurations at $M_\infty = 0.20$, and $Re = 9.0 \times 10^6$ [63].

generation method of Mavriplis [65]. The modeling includes accurate representation of the blunt trailing edges on each element. Representative results obtained with this method are depicted in Fig. 22 for the three-element airfoil with $30°$ slat deflection and $30°$ flap deflection in two slightly different configurations at $M_\infty = 0.2$ and $Re = 9.0 \times 10^6$. These two configurations, $N$ and AG, differ only in the flap rigging with $N$ and AG having an overlap/gap of $0.0127c/0.025c$ and $0.01c/0.01c$, respectively. In both the computations and the experiment, the $N$ configuration attains higher lift coefficients than the AG configuration. Overall good agreement is obtained between the results measured in the NASA Langley LTPT facility (see Section 7 for more information on this facility) and FUN2D.

Probably one of the most extensively applied methods for the analysis and design of multi-element high-lift airfoils is the Reynolds-averaged Navier–Stokes solver INS2D. Rogers et al. [47–52] have published a wide array of papers demonstrating the effectiveness of this method. Its drawback is that it is based on the incompressible equations and, hence, the important effect of Mach number on maximum lift coefficient cannot be evaluated. The method solves the governing equations on structured overset meshes as illustrated in Fig. 23 for a three-element airfoil. For this case the complete mesh consists of a total of five overset meshes: main element mesh which extends into the farfield, slat mesh, flap mesh, main-element cove mesh, and flap wake mesh. Representative results obtained with this method

are depicted in Fig. 24 for the three-element airfoil with $30°$ slat deflection and $30°$ flap deflection in two slightly different configurations at $Re = 9.0 \times 10^6$. These two configurations differ only in the flap rigging; an overlap/gap of $0.010c/0.0132c$ versus $0.010c/0.0218c$. The computations provide an excellent prediction of the loss in lift due to the change in flap rigging at the lower angles of attack. However, the prediction of the effect of flap rigging on the maximum lift is off. The consistent and accurate prediction of the maximum lift coefficient for multi-element airfoils remains a problem for RANS methods. (However, one should keep in mind that maximum lift flow conditions are typically 3D in nature and as such one should question the capability of a 2D analysis to predict maximum lift correctly.) Given this lack of consistency, Greenman et al. [49–51] implemented a so-called pressure difference rule to provide a 'sanity check' on the maximum lift predictions obtained with INS2D. The semi-empirical pressure difference rule, developed by Valerezo and Chin [66], allows for the prediction of maximum lift based on the pressure difference between the suction peak and trailing edge. Once this pressure difference reaches a certain value that is Reynolds number and Mach number dependent, maximum lift is marked.

In this section the focus has been on the prediction of lift. A critical assessment of the drag prediction capabilities of two-dimensional interaction and Navier–Stokes methods is presented in an earlier paper [67]. The results in [67] indicate that for single-element airfoils at attached flow conditions the drag can be very accurately predicted. To attain this accuracy, the flow solutions must be obtained on sufficiently dense meshes with large number of mesh points not only near the
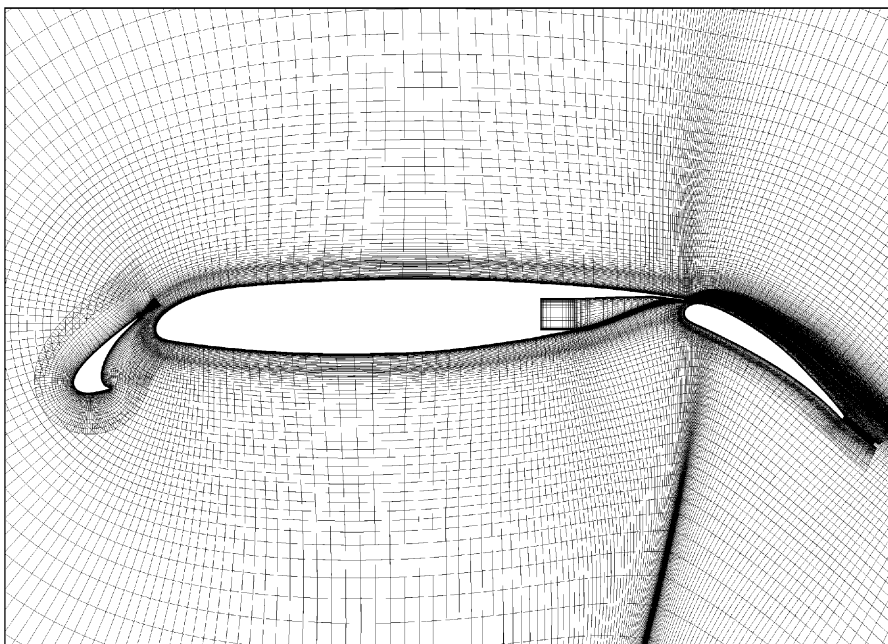
Fig. 23. Near view of structured overset mesh about three-element airfoil.
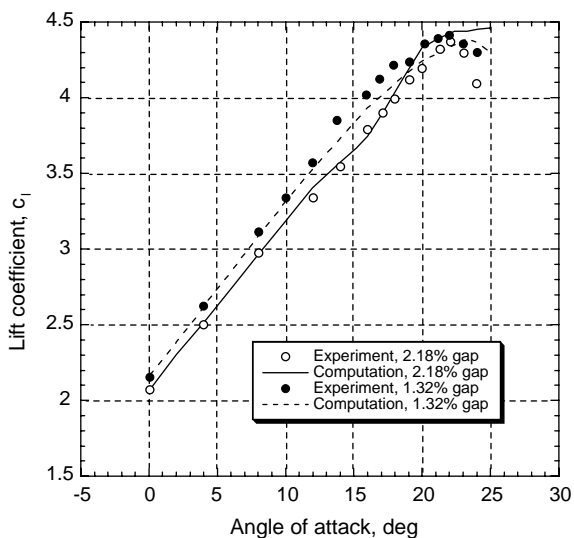


Fig. 24. Comparison of computed and experimental results for three-element airfoil in two different configurations at $M_\infty = 0.20$, and $Re = 9.0 \times 10^6$ [48].

airfoil surface to capture the boundary-layer development but also downstream of the airfoil to capture the wake. Given a sufficiently dense mesh, drag predictions based on surface integration are also shown to be consistent with those based on wake integration. For single-element airfoils with separated flows and multi-element airfoils drag predictions based on RANS solutions appear to be much less accurate. One reason for this lack of accuracy is related to deficiencies in the turbulence models. Another reason may be the high levels of numerical dissipation inserted in the solutions to facilitate convergence for these more complex flow problems.

### 6.2. Three-dimensional methods

The above list of methods and applications demonstrates that 2D RANS simulations are rapidly making inroads into the high-lift system design process. However, much slower progress is reported when it comes to RANS simulations for wings and complete aircraft in the high-lift configuration and relatively few examples have been published. The main reason for this is the time consuming process of creating a mesh that provides reliable predictions for complex 3D geometries such as complete transport aircraft in the high-lift configurations. Another reason is the amount of CPH time required for 3D RANS simulations. However, providing insight into the performance characteristics of aircraft in the takeoff and landing configuration early in the development process is one of the major areas where RANS methods can prove their worth compared to less time consuming, lower-fidelity 3D methods, as well as to wind-tunnel testing. Recently, several papers were presented at the AIAA Applied Aerodynamics Conference in Denver, Colorado, that give a good overview of the predictive capabilities of Reynolds-averaged Navier–Stokes method as applied to subsonic high-lift

aircraft. A group of researchers at the NASA Ames Research Center and the Boeing Company applied the overset-structured method OVERFLOW to simulate the flow fields of several aircraft in the high-lift configurations including a Boeing 777-200 and a High Wing Transport with externally blown flaps [68–70]. Rudnik et al. [71] applied the block-structured FLOWer method and the unstructured Tau method to simulate the flow about an Airbus 320. Takallu [72] applied the block-structured TLNS3D method to simulate the flow field of an energy efficient transport (EET) model. In addition to these methods, Mavriplis and Pirzadeh [73–76] have extensively used their unstructured mesh generation method and the NSU3D flow solver to simulate flows about several wings and aircraft. Also, Berkman et al. [77] have used the structured grid flow solver CFL3D for detailed flow field studies of the flap system of the EET.

The state-of-the-art in complete geometry to lift- and drag-analysis capability for complicated three-dimensional high-lift configurations is represented by the methodology of Mavriplis and Pirzadeh [73–75]. Their methodology is based on unstructured meshes to enable rapid grid generation for complicated geometries and a RANS solver that uses an agglomeration multigrid algorithm to enhance convergence and is optimized for massively parallel computers. Recently, they published some impressive results for a wing-body in the high-lift configuration (EET) at $M_\infty = 0.20$ and $Re = 1.6 \times 10^6$. The wing-body configuration has an aspect ratio 10 wing, a leading-edge sweep angle of $28.8°$, and a multi-element high-lift system in the takeoff position. The high-lift system consists of a leading-edge device at a deflection angle of $50°$, a vane at $15°$, and a flap at $30°$. A thrust gate separates the inboard and outboard flaps. For this case the coarse mesh consists of $3.1 \times 10^6$ vertices and $18.2 \times 10^6$ tetrahedra whereas the fine mesh consists of $24.7 \times 10^6$ vertices, $53 \times 10^6$ tetrahedra, $31 \times 10^6$ prisms and 281,000 pyramids. Figs. 25 and 26 show the comparisons between computed and experimental lift curve and drag polar, respectively. The lift is overpredicted by both sets of computations. The maximum lift point appears slightly better predicted by the coarse mesh than the fine mesh computations. Post-stall the computations fail to obtain steady solutions on either mesh. The average as well as the minimum and maximum values are shown in the figures indicating the large variations in the computational predictions at these conditions. Overall the agreement is quite good given the geometric complexity of the configuration. More recently, the propulsion system has been included in the computational model and Figs. 27 and 28 provide close-up views of the EET wing–pylon–nacelle and the details of the pylon–slat region.

A representative example of a block-structured solution methodology capability for complicated three-
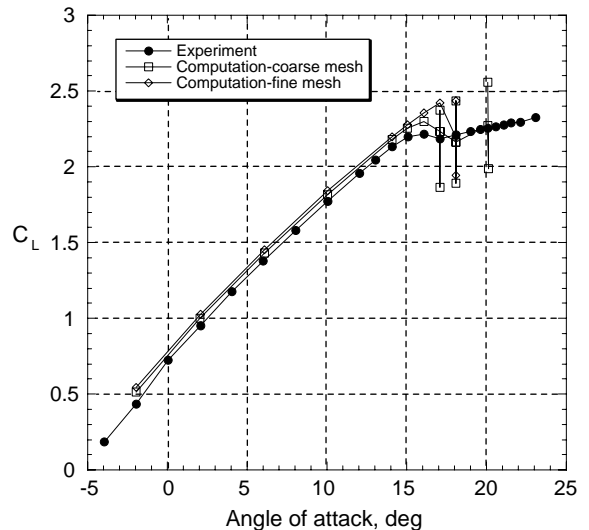


Fig. 25. Comparison of computed and experimental lift curves for wing-body configuration (EET) in high-lift configuration at $M_\infty = 0.20$, and $Re = 1.6 \times 10^6$ [75].
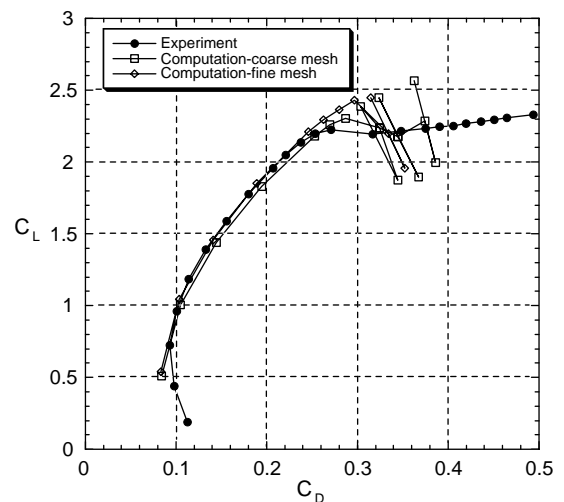


Fig. 26. Comparison of computed and experimental drag polars for wing-body configuration (EET) in high-lift configuration at $M_\infty = 0.20$, and $Re = 1.6 \times 10^6$ [75].

dimensional high-lift configurations is provided by Rudnik et al. [71,78]. Rudnik et al. [71,78] apply the FLOWer code to solve the flow about an Airbus 320 type configuration at a takeoff flap setting of $20°$. In Figs. 29 and 30 the Navier–Stokes results are compared against the wind tunnel results obtained in the DNW facility (see Section 7 for more information on this facility) at $M_\infty = 0.22$ and $Re = 2.0 \times 10^6$. In the lift coefficient range important for second segment climb
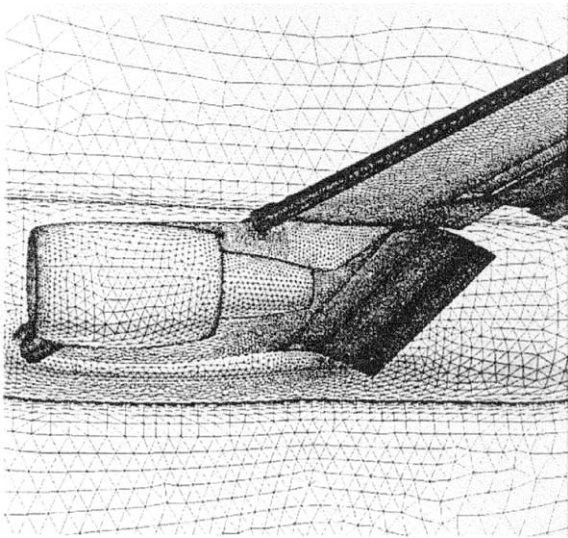
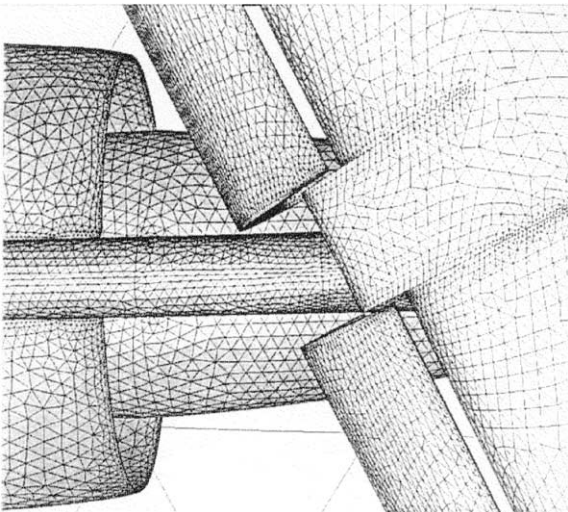Fig. 27. Close-up view of surface mesh of EET wing–pylon–nacelle [73].



Fig. 28. Close-up view of surface mesh details in EET pylon–slat region. [73].
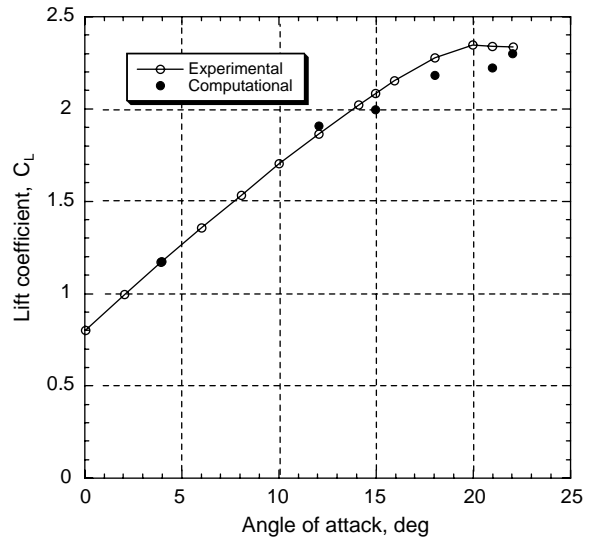


Fig. 29. Comparison of computed and experimental lift curves for wing-body model in takeoff configuration at $M_\infty = 0.22$, and $Re = 1.6 \times 10^6$ [71].
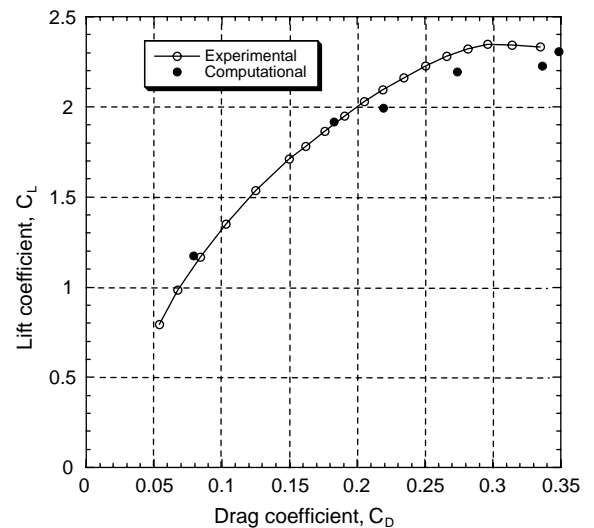


Fig. 30. Comparison of computed and experimental drag polars for wing-body model in takeoff configuration at $M_\infty = 0.22$, and $Re = 1.6 \times 10^6$ [71].

operation ($C_L \approx 1.7$), good correlation is obtained between the measured and computed lift and drag results. However, at higher angles of attack lift is underpredicted whereas drag is overpredicted. Rudnik et al. [71] link this discrepancy to premature flow separation in the region of the thrust gate in the numerical predictions. The authors also applied an unstructured grid method that gave similar results to the structured method. However, the unstructured methodology appears to be favored "due to the high potential in efficient and accurate grid generation and adaptation of the grid to local flow phenomena, that are of great importance especially for high-lift investigations" [71].

Another methodology that lends itself to the solution of complicated flow problems is the overset, or chimera, structured grid method. The flow solver OVERFLOW is based on this approach and Rogers et al. [79,80,68,70,69] have applied it to obtain flow simulations for several high-lift configurations including an
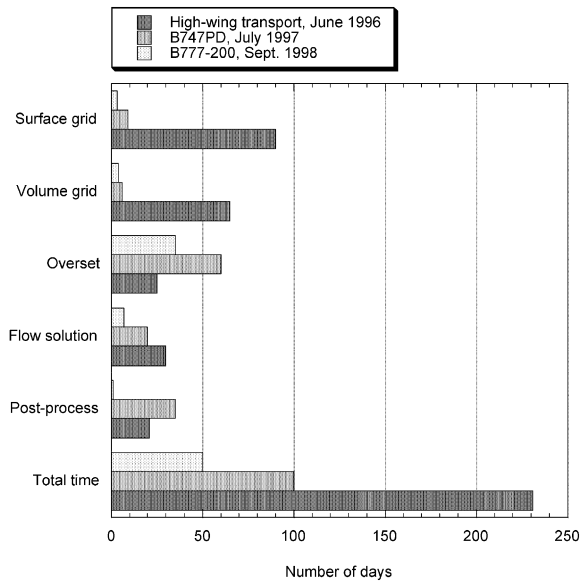
Fig. 31. Comparison of time required to obtain a RANS solution using structured overset grid methodology [68].

early design version of the Boeing 747, a high wing transport with externally blown flaps, a simplified 3D high-lift wing, and a Boeing 777-200. Most impressive is their effort to reduce the time required to generate the surface and volume grids, to obtain the flow solution, and to post-process the data. Through a focused multi-year effort they were able to reduce the time required from a CAD definition to an analyzed solution to 50 days and to 5 days for a minor design change to an analyzed solution. Fig. 31 illustrates the improvements made in this process. Note that the corresponding meshes are substantial, ranging from 8.9 million points for the B747PD to 22.4 million points within 79 overset zones for the B777-200 in the landing configuration. For the latter problem the computed lift coefficient at a typical approach angle of attack of 8° was within 1.2% of the wind-tunnel measured value and the drag coefficient within 2.6%.

It may be worth noting that the above 3D RANS methods do not include boundary-layer transition models and most if not all of the computational studies assume fully turbulent flow conditions.

These 3D Navier–Stokes results demonstrate that the tools to accurately analyze complicated three-dimensional high-lift configurations are slowly becoming available. However, cycle times on the order of 50 days (or even 5 days for a design perturbation) are still too long for most 3D high-lift design problems. Hence, reduced-order methods such as lifting surface and panel methods with or without viscous effects provided by boundary-layer methods or airfoil viscous-flow codes remain the standard in many cases.

Until recently the only methodology available for the aerodynamic analysis of complex 3D geometries was the panel method. Panel methods such as the Douglas method [81], PAN AIR [82], VSAERO [83], and PMARC [84] are general three-dimensional boundary value solvers for the Prandtl–Glauert equation. The advantage of this type of method is that a surface flow solution for complex high-lift configurations can be obtained rapidly. The disadvantage is that it is an inviscid solution unless the panel method is coupled to a boundary-layer method. Tinoco et al. [85] discuss the application of the higher-order panel method PAN AIR in the design and analysis of the B737-300 in the high-lift configuration. Yip et al. [27] discuss the application of the low-order methods PMARC to analyze the pressure distribution on the B737-100 wing in the high-lift configuration. (Also see Dodbele [86] for a VSAERO application.) PMARC includes a boundary-layer routine to account for viscous effects; however, this routine based on the momentum-integral equation was deemed to be not accurate enough for the present problem and, therefore, only inviscid calculations were conducted. Several issues were addressed in the surface-grid generation process to maximize the accuracy of the flow-field solutions, as discussed by Edge and Perkins [87]. In order to evaluate the effect of trailing-vortex-sheet deformation and rollup, three different wake models were investigated. Overall, correlation of experimental and computational data revealed that panel methods are able to predict reasonably well the pressure distributions of the multi-element wing for a range of angles of attack. The computational model includes all high-lift devices; the Krüger flap inboard of the engine, the three outboard slats, and both sets of triple-slotted flaps. In Fig. 32 a comparison of the measured and computed pressure distributions at WBL 324 is shown for $\alpha = 8°$. The predicted pressures agree fairly well with the flight measured data. However, suction pressures in regions dominated by viscous effects are largely over-predicted, as expected. Also, the second leading-edge suction peak in the pressure distribution of the main element (due to the surface discontinuity where the slat nests in cruise) is not predicted because of a lack of resolution in the surface grid. The effect of a flow-through nacelle on the pressure distribution was also studied and shown to be small [87].

Although many if not all of the panel methods incorporate integral or finite-difference boundary-layer methods to predict the viscous effects, the viscous/inviscid coupling is too weak to predict stall. For this reason Valerezo and Chin [66] combined a panel method [81] and a semi-empirical pressure difference rule (PDR) to obtain remarkably accurate maximum lift predictions for complex 3D configurations. The PDR is a refinement of an empirical method first described by Loftin and von Doenhoff [88]. Fig. 33 shows the pressure difference rule
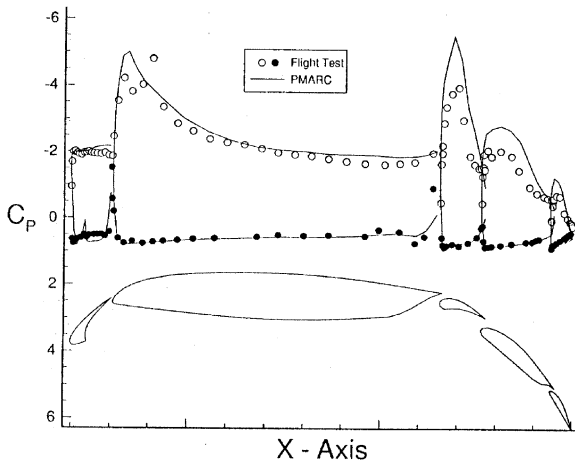
Fig. 32. Comparison of flight measured pressure distribution and inviscid prediction at WBL 324, B737-100, 40° flaps, $\alpha = 8°$ [27].
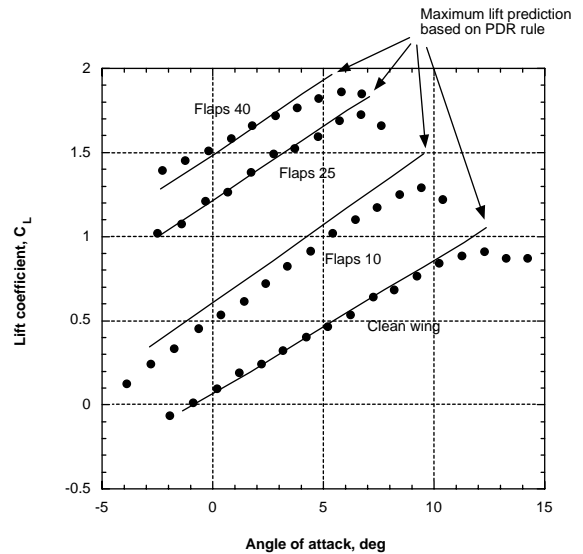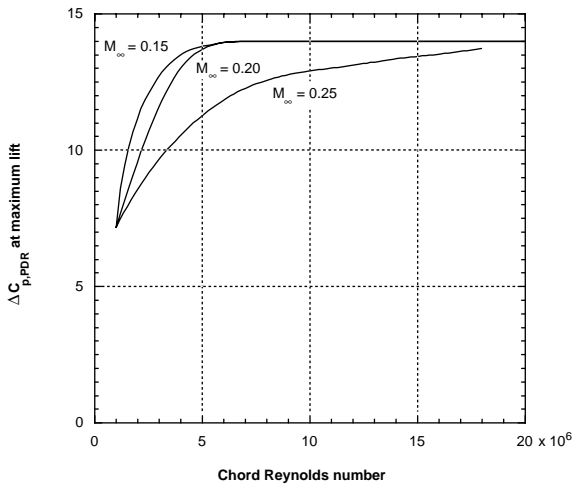


Fig. 33. Pressure difference rule (PDR) for maximum lift prediction [66].

used to predict stall where

$$\Delta C_{p,\text{PDR}} = |C_{p,\text{suction-peak}} - C_{p,\text{trailing-edge}}|$$

and this rule is applied on each element in the case of a multi-element system. Valerezo and Chin [66] show maximum lift predictions for several configurations including the RAE swept-wing model [89]. In Fig. 34 lift curves are shown for the RAE model in various high-lift configurations. In all cases fair to good agreement with the wind tunnel results were obtained. However, note that the flap deflection angles specified in the inviscid panel method calculation were reduced from the geometric flap angles to account for the viscous effects on flap effectiveness. This is common practice in panel



Fig. 34. Comparison of wind-tunnel measurements and surface panel method + PDR predictions for RAE wing with flap [66].

method based high-lift calculations where it should be emphasized that this flap reduction information is often unavailable in the preliminary design stages of a high-lift system.

In order to be able to calculate the lift of a three-dimensional multi-element wing configuration over the entire angle of attack range without the need of modifying the geometric flap angles to account for viscous effects, several researchers have developed so-called quasi-three-dimensional viscous methods. These methods combine two-dimensional viscous airfoil data with three-dimensional inviscid wing data to allow for the calculation of the aerodynamic characteristics over the entire angle-of-attack range including the maximum lift condition. These methods are non-linear to account for the non-linear variation in lift with angle of attack at separated flow conditions. More importantly, such methods are both fast and economical and this makes them attractive for use in high-lift system design and development. Brune and McMasters [32] discuss this category of methods and present some results. More recently, Jacob et al. [90–93], Wakayama and Kroo [94], and Van Dam et al. [95] have presented further developments. The work by the latter is briefly reviewed and some results obtained with this method are presented.

Van Dam et al. [95] use a modified lifting-line method based on theory originally developed by Weissinger [96] and later simplified by Campbell [97] and Blackwell [98] to compute the load distribution in subsonic compressible flow of arbitrary wings and lifting surface arrangements. The simplification involves replacing the continuous lifting line of varying strength by a discrete
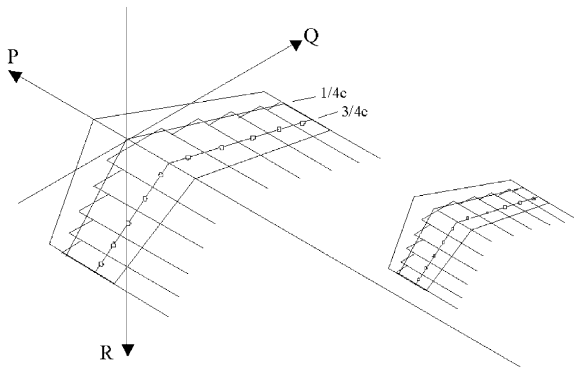
Fig. 35. Distribution of horseshoe vortices over a multiple lifting-surface configuration [98].

system of horseshoe vortices, each of which is of constant strength. The resulting method, called finite-step method or vortex step method [99], allows one to couple sectional (2D) viscous results with inviscid wing (3D) theory in order to determine the total aerodynamic coefficients for configurations including wings with dihedral, endplates/winglets, pylons, and biplanes, joined-wings, etc. The present method has advantages over the traditional panel or vortex lattice methods because it incorporates the critical viscous nature of high-lift devices and is also significantly faster since the chordwise panels are modeled as single 'strips'.

The modified Weissinger method represents the lifting surfaces by a system of rectangular horseshoe vortices placed along the quarter-chord line of the lifting surfaces as illustrated in Fig. 35. The load distribution is calculated by solving a linear system of equations that enforce a flow tangency condition at the specified control points. For subsonic flow, the effects of Mach number on lift-curve slope and control point position are taken into account using the Prandtl–Glauert equation. The lift is integrated directly from the calculated load distribution. The induced drag is calculated based on the velocities in the Trefftz plane. If the profile drag of the individual airfoil sections is available, it can be integrated along the span of the wing and added to the induced drag to get the total drag of the configuration. The total pitching moment is calculated by translating the sectional pitching moment to a wing reference line and integrating along the span of the wing.

Although the modified Weissinger method reduces the lifting surfaces to flat plates, various airfoil shapes, including high-lift configurations, can be successfully modeled. This is done by adjusting the location of the control points to reflect the proper lift-curve slope and the panel incidence angles to reflect the zero-lift angle of attack of the airfoil. Using this methodology, a variety of test cases have been analyzed to validate the three-dimensional portion of the high-lift module [95].

The modified Weissinger method is capable of analyzing complete aircraft lifting surface configura-tions, including the main wing with high-lift system, horizontal tail and/or canard, and vertical tail. The geometry of these surfaces can include sweep, taper, twist, and dihedral. Additional features that have been added to the three-dimensional portion of the high-lift module include a simple fuselage model, a non-linear $C_{L_{max}}$ prediction routine, and a wind-tunnel wall model based on mirror images.

The equations for the modified Weissinger method were derived assuming the sections containing the control point and the point at which the load is determined lie in a line parallel to the free-stream direction. Thus, any considerations of the sectional characteristics can be applied only to sections lying along these lines. However, simple sweep theory suggests that it is more accurate to make the controlling airfoil section one that lies on a line normal to the quarter-chord line. This theory suggests that 2D to 3D corrections are required for swept wings with high-aspect ratios in order to get the aerodynamic characteristics for a controlling section oriented in the free-stream direction.

In reality, for a finite wing, the orientation of the 'correct' controlling airfoil section will change over the span of the wing and is probably somewhere between the free-stream and normal direction. An investigation of the most appropriate sweep correction, if any, was conducted by Paris [100]. In all cases considered it was found that *no* sweep correction was required. Voogt [101] using a vortex lattice code coupled with two-dimensional viscous results to calculate the performance of swept wings also reaffirmed this finding. However, particularly for highly swept wings with leading-edge devices some sweep correction is likely needed.

The non-linear method for predicting $C_{L_{max}}$ couples the modified Weissinger method with 2D viscous flow calculations (or experimental data). At a minimum, 2D viscous data is required for the wing root and wing tip sections. If there exists a significant variation in the spanwise airfoil geometry, such as is the case of high-lift configurations and most cruise wings, viscous data for additional stations along the wing should be used. The viscous data for each defining airfoil section is compiled into a single data file that is read by the high-lift module. The lift-curve slope, $C_{l_z}$, and zero-lift angle of attack, $\alpha_0$, are then calculated for each section. This information is used in the present method to calculate the initial load distribution from which the local coefficient of lift is calculated for each spanwise station. After this initial 3D calculation, the following iterative procedure is per-formed for each angle of attack being examined:

1. Calculate the effective local angle of attack for each station using:

$$\alpha_{local} = \frac{C_{l_W}}{C_{l_z}} + \alpha_0 - \Delta\alpha_{visc},$$

where the local lift coefficient, $C_{l_w}$, is calculated for each station from the bound vortex strength and, $\Delta\alpha_{visc}$, is the viscous correction angle (see step 3) which is initially equal to zero.

2. Find $C_{l_{visc}}$ at the local angle of attack, $\alpha_{local}$, by interpolating the 2D viscous section input data.

3. If $|C_{l_{visc}} - C_{l_W}| > \varepsilon$, with a typical value for $\varepsilon = 0.01$, determine the appropriate viscous correction angle for each section such that at the local angle of attack the lift coefficient of the corrected section equals $C_{l_{visc}}$ using the following:

$$\Delta\alpha_{visc} = \frac{C_{l_{visc}} - C_{l_W}}{C_{l_\alpha}}.$$

See Fig. 36 for a graphical description of $\Delta\alpha_{visc}$.

4. Adjust the $\alpha$-distribution (left-hand side of system of equations in the modified Weissinger method) by the

appropriate local viscous correction angle, $\Delta\alpha_{visc}$, and calculate the resulting load distribution.

5. Repeat steps 1–4 until $|C_{l_{visc}} - C_{l_W}| < \varepsilon$ for all spanwise stations.

This iterative procedure is performed for a complete angle-of-attack sweep. The maximum lift coefficient and stall angle can easily be determined from the resultant lift curve. Several validation test cases used in the validation of the $C_{L_{max}}$ prediction routine are presented and discussed next.

Van Dam et al. [95] present several test cases that depict the capabilities and accuracy of the hybrid flow solution method and in particular the $C_{L_{max}}$ prediction routine. One test case is the F-29 swept cruise wing configuration shown in Fig. 37 [5]. The wing has 21° of sweep at the quarter-chord, aspect ratio 10, and taper ratio 0.23. The method utilized 2D aerodynamic data at nine different spanwise locations, as indicated in Fig. 37, for the non-linear $C_{L_{max}}$ calculations. The correlation with experimental data is excellent and can be seen in Fig. 38. The good agreement between the experimental data and the present prediction demonstrates that the non-linear $C_{L_{max}}$ prediction routine works very well for cruise wing configurations, provided accurate 2D sectional data is available.

A second test case was selected in order to validate the capabilities of the method for configurations containing multiple lifting surfaces. In this configuration, two rectangular planforms utilizing the LS(1)-0413 airfoil section make up a wing-canard configuration as seen in Fig. 39 [102]. This configuration was tested in the NASA Ames 7 ft × 10 ft tunnel. In the arrangement discussed here, the wing and canard are 0.48 m ($1.6c_{wing}$) apart horizontally and the wing is 0.15 m ($0.5c_{wing}$) below the canard. Two-dimensional sectional data were obtained using the Reynolds-averaged Navier–Stokes solver INS2D [47,48]. Due to the sensitivity of high-lift
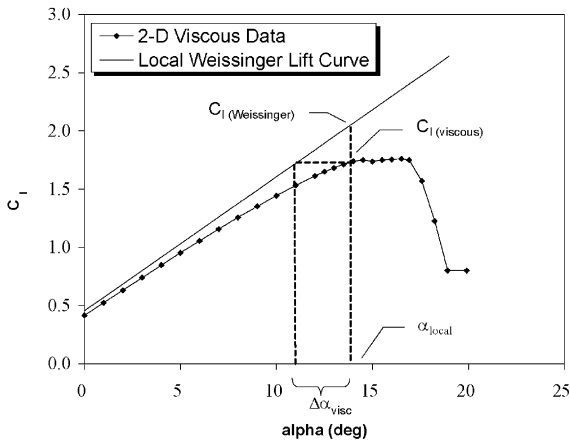


Fig. 36. Definition of viscous correction angle as part of non-linear $C_{L_{max}}$ prediction routine.
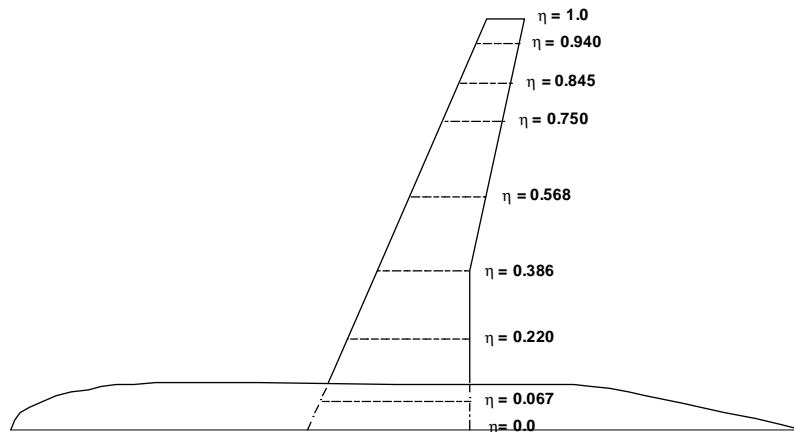


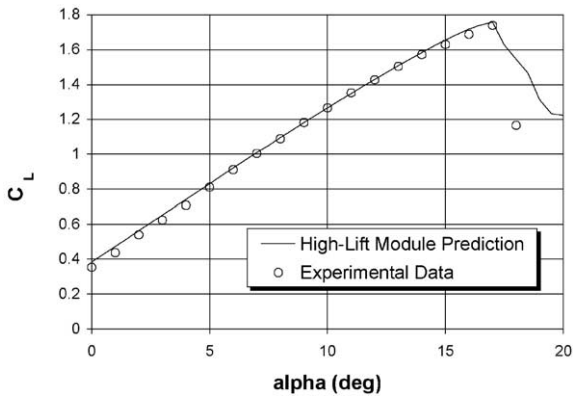Fig. 37. Wing-body configuration with 2D aerodynamic data specified at nine stations indicated.

Fig. 38. Comparison of predicted and measured lift curves for wing-body configuration at $M_\infty = 0.19$, $Re_{MAC} = 5.0$ million.



Fig. 40. Lift results for the close-coupled wing-low canard test case, $Re = 1.4$ million.
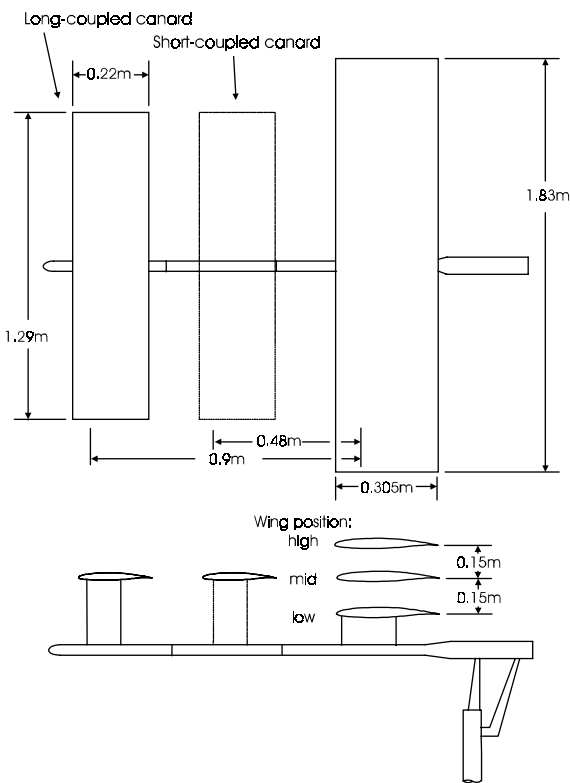


Fig. 39. Geometry definition of the canard test case [102].

aerodynamics to boundary-layer transition, some attention must be paid to transition location on the airfoil elements. Recently, a transition prediction algorithm has been incorporated into the INS2D flow solver that makes it possible to determine the onset of transition automatically as the flow solution converges [103,104]. This methodology identifies several transition mechanisms. In two-dimensional airfoil flows, where surfaces are generally smooth and freestream turbulence levels are low, transition is governed by Tollmien-Schlichting (TS) instability, laminar separation, or turbulence contamination [105]. The latter mechanism is often overlooked, but can be important when, for instance, the flap boundary layer is contaminated by the wake of the main element and/or the slat [24]. The method is described in more detail by Brodeur and van Dam [103,104]. Lift results are shown in Fig. 40. These results demonstrate the accuracy of the method for multiple lifting surface configurations.

The final test case is that of the RAE 1372 tested at the No. 2 $11\frac{1}{2} \times 8\frac{1}{2}$ ft tunnel at Farnborough [89]. This configuration consists of a swept wing evaluated in the clean configuration as well as with full and 80% span flaps deflected 10° and 25°. The wing sweep angle is 28° at the quarter-chord, the aspect ratio is 8.35 and the taper ratio is 0.35. Again, 2D sectional data were obtained using INS2D and the transition prediction method discussed previously. It is interesting to note that the flap coordinates provided in the experimental report were quite coarse and required that the leading edge region be refined with a cubic spline. This refinement introduces some uncertainty into the 2D predictions as the proper geometry is unknown in this critical portion of the airfoil. Fig. 41 illustrates the accuracy of lift predictions for the configuration with full-span flaps whereas Fig. 42 presents results for the 80% span flap case. There is some discrepancy in the results for the 25° flaps setting which may be due to the aforementioned flap coordinate issue. The proper amount of required geometry refinement was not known
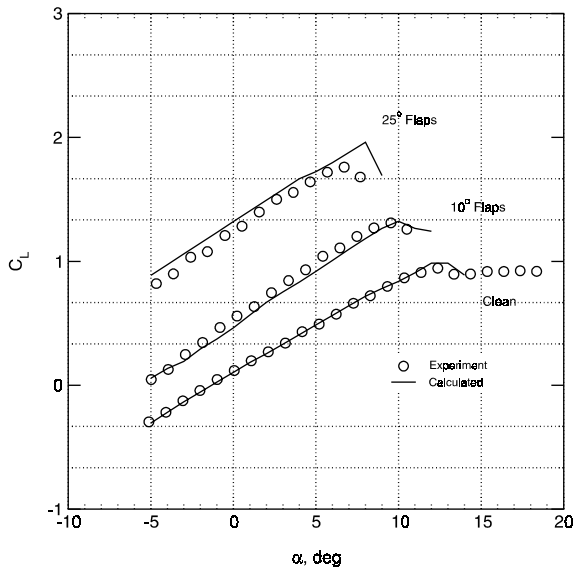
Fig. 41. Effect of full-span flaps on the RAE 1372 test case, $Re = 1.35$ million, $M_\infty = 0.233$.
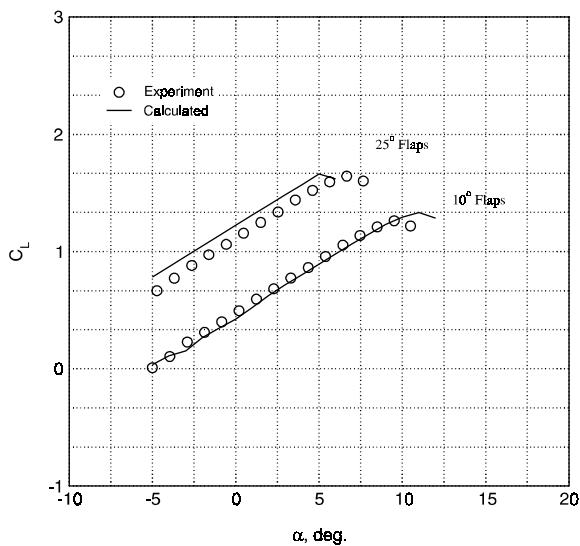


Fig. 42. Effect of 80% span flaps on the RAE 1372 test case, $Re = 1.35$ million, $M_\infty = 0.233$.

and may not reflect the actual test case geometry to within a negligible margin of error. Nonetheless, these results illustrate that the method is capable of highly accurate results for realistic geometries in the clean and high-lift configurations.

In summary, the flow solver that is part of the high-lift module produces excellent results for cruise and high-lift wings including wings with part-span flaps. In addition, the wind-tunnel wall model and fuselage models are

working quite well. It provides an excellent compromise between computing time and accuracy for calculating the high-lift performance of an aircraft at the conceptual and preliminary design stages.

## 7. Wind-tunnel testing

Although computational methods for high-lift design and analysis are becoming more capable and faster, wind tunnel testing remains critically important in most high-lift system development programs. A large number of facilities are available around the world. However, this section will focus on the high-Reynolds-number facilities used by airframe manufacturers for high-lift development work. In addition to these more expensive facilities, many manufacturers also conduct exploratory type of tests in smaller lower-Reynolds-number facilities such as the Deutsche Airbus Low-Speed Tunnel [4], the University of Washington tunnel (UWAL) [29], the Walter H. Beech Memorial Wind Tunnel at Wichita State University, and the Glenn L. Martin Wind Tunnel at the University of Maryland, among other facilities.

Three different types of tunnels are typically used in high-lift testing. First, there is the atmospheric wind tunnel. This type of tunnel tends to be relatively large, allowing for the testing of large-scale models at relatively high Reynolds numbers. Higher airspeeds in the test section result in even higher Reynolds numbers but also in higher Mach numbers. This coupling of viscous (scale) and compressibility effects is undesirable and can make the extrapolation of maximum lift data from tunnel Reynolds numbers to flight Reynolds numbers problematic [106]. Mainly because of the need to de-couple scale and compressibility effects, high-lift system designers tend to favor testing in a pressurized tunnel. In this type of tunnel, Mach number and Reynolds number can be varied independently within the bounds of the tunnel operating limits as illustrated in Fig. 43 for the ONERA F1 tunnel. For a given Mach number, increasing the stagnation pressure increases the Reynolds number. However, a downside of this is that this increase in Reynolds number is achieved by increasing dynamic pressure. The aerodynamic performance of multi-element high-lift systems is strongly dependent on flap gap and overlap as well as flap deflection angle. Changes in dynamic pressure causes changes in aerodynamic loading, and this may affect the spacing and orientation of the flap system as a result of aeroelastic deformations. These aeroelastic effects are undesirable because they may distort Reynolds number trends, making the extrapolation of maximum-lift data from tunnel to flight Reynolds numbers problematic. This brings up the need to test at cryogenic conditions; i.e., at low ambient temperatures which reduces the viscosity and speed of sound and increases
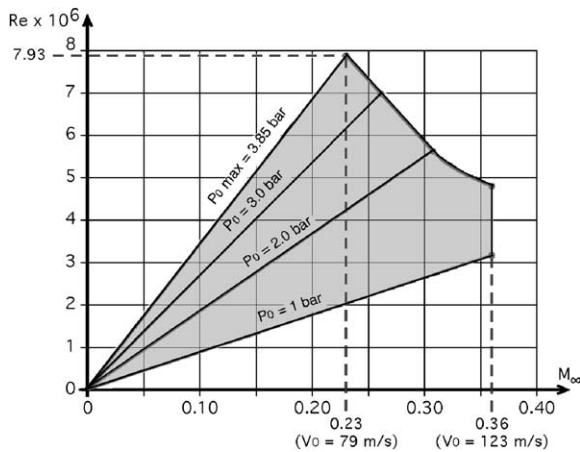
Fig. 43. Operating range for ONERA F1 pressure tunnel. Reynolds number is based on reference length = test-section-cross-sectional-area$^{0.5}$/10 = 0.397 m (1.302 ft) at stagnation temperature of 288 K (chart courtesy of ONERA).



Fig. 44. Multi-element airfoil model mounted in the LTPT test section (photo courtesy of the NASA Langley Research Center).



Fig. 45. Semispan EET model as tested with 2D standoff in the 14 ft × 22 ft tunnel (photo courtesy of the NASA Langley Research Center).

the density. Testing in a cryogenic pressure tunnel allows for the de-coupling of scale, compressibility, and aeroelastic effects. Secondly, for most aircraft it allows testing at flight Reynolds numbers thereby eliminating the need for extrapolating tunnel results. However, testing at high-pressure low-temperature conditions is expensive and time consuming and the high-Reynolds-number cryogenic environment can lead to surface contamination problems [107].

One well-known high-lift testing facility is the low-turbulence pressure tunnel (LTPT) at the NASA Langley Research Center. This tunnel has been extensively used to study the aerodynamic performance characteristics and detailed flow phenomena of single- and multi-element airfoils. It is a single-return, closed-circuit tunnel that can be operated at stagnation pressures from 1 to 10 atm. It has a unit Reynolds number range of $0.1–4.6 \times 10^6 \, \text{m}^{-1}$ $(0.4–15 \times 10^6 \, \text{ft}^{-1})$ and a Mach number range from 0.05–0.5. It has a rectangular test section with a width of 0.9 m (3 ft) a height of 2.3 m (7.5 ft) and a length of 2.3 m (7.5 ft) allowing the testing of airfoils with a chord of approximately 0.6 m (2 ft). The contraction section leading up to the test section has an area ratio of 17.6:1. In addition to this relatively large contraction ratio it contains nine fine-mesh turbulence reduction screens resulting in a low turbulence level in the test section [108]. Fig. 44 depicts a multi-element airfoil in the test section [109]. The model is mounted horizontally and the photo clearly depicts the sizeable brackets required to support the slat and the flap at the high dynamic pressure conditions encountered in pressurized tunnels.

A second high-lift facility at the NASA Langley Research Center is the 14 ft × 22 ft subsonic tunnel (formerly the 4 m × 7 m tunnel) which is used for testing the aerodynamic characteristics of all types of aircraft and rotorcraft. This closed-circuit atmospheric tunnel has a test section width of 6.6 m (21.75 ft), a height of 4.4 m (14.5 ft), and a length of 15.2 m (50 ft). It is capable of speeds up to 106 m/s (206 knots) with corresponding unit Reynolds number of $7.2 \times 10^6 \, \text{m}^{-1}$ $(2.2 \times 10^6 \, \text{ft}^{-1})$ and Mach number of 0.31. The tunnel can be operated with closed test section walls (which may be slotted) or with the sidewalls and ceiling raised resulting in an open test section. It has a contraction ratio of 9:1 and includes perforated grid, screens, and honeycomb to further improve the flow quality. Fig. 45 depicts the EET

semi-span model with its four-element high-lift system deployed in the test section of this tunnel [110,111].

For the testing of complete aircraft in the high-lift configuration, the large low-speed facility (LLF) which is one of the eight wind tunnels operated by Duits-Nederlandse Wind Tunnel (DNW) provides an oft-used venue for high-lift investigations. This atmospheric tunnel has a test section with a width of 6 m (20 ft), a height of 8 m (26 ft), and a length of 20 m (66 ft). It is capable of generating a maximum speed of 116 m/s (225 knots) which corresponds to a unit Reynolds number of $7.9 \times 10^6 \, \text{m}^{-1}$ ($2.4 \times 10^6 \, \text{ft}^{-1}$) and a Mach number of 0.34. This translates into a typical reference chord Reynolds number of approximately $3 \times 10^6$ for an aircraft model with a span of 5 m (16 ft) at a Mach number of 0.2. For a large facility it has a relatively large contraction ratio of 9:1 and this contributes greatly to its excellent low-turbulence flow characteristics. Issues such as second-segment climb performance characteristics including turbine-powered simulators (TPS) and high-lift performance in ground effect tend to be investigated in this tunnel [4,112]. Fig. 46 shows a 1:16.2 scaled model of the A3XX (now named A380) in the landing configuration being tested in ground proximity above the moving belt ground plane of the LLF. The model is equipped with compressed air driven simulators. The drive air is conducted along the dorsal sting support and via a reaction-free bridging system over the internal balance to the wing and the engine pylons. The span of the model is approximately 5 m (16 ft) and it weighs approximately 1.5 tons. The support system allows the positioning of the model up to a few millimeters above the belt.

The 40 ft × 80 ft test facility is the smaller closed-return part of the National Full-Scale Aerodynamics Complex (NFAC) at the NASA Ames Research Center. This atmospheric tunnel has a test section width of 24 m (79 ft), height of 12 m (39 ft), and length of 24 m (80 ft) making it ideal for the testing of large- or full-scale

models. It is capable of a maximum speed of approximately 143 m/s (278 knots) with corresponding unit Reynolds number of $9.7 \times 10^6 \, \text{m}^{-1}$ ($3.0 \times 10^6 \, \text{ft}^{-1}$) and Mach number of 0.42. Recently this tunnel underwent an aeroacoustic modernization that includes a 1.1 m (3.5 ft) deep acoustic liner around the test section. With the new liner, 85–95% of the acoustic energy is absorbed giving it unique acoustic testing capabilities. A large-scale semi-span model of the B777 was recently tested in this facility to pinpoint airframe noise sources and evaluate noise alleviation techniques for the airplane in the high-lift configuration. Fig. 47 shows a photo of a T-39 airplane in the test section of the 80 ft × 120 ft facility of the NFAC.

The 12-ft pressure wind tunnel at the NASA Ames Research Center is a closed-return facility primarily used for high-Reynolds-number testing of commercial and military airplanes at high-lift and high-angle-of-attack conditions. It can be operated at stagnation pressures from 0.1 to 6 atm. It is capable of a maximum unit Reynolds number of $43.3 \times 10^6 \, \text{m}^{-1}$ ($13.2 \times 10^6 \, \text{ft}^{-1}$) at a Mach number of 0.42 and a maximum Mach number of approximately 0.55 at a unit Reynolds number of $21.3 \times 10^6 \, \text{m}^{-1}$ ($6.5 \times 10^6 \, \text{ft}^{-1}$). It has a test-section diameter of 3.7 m (12 ft) with 1.2 m (4 ft) wide flats on the ceiling, floor, and side walls, and a test-section length



Fig. 47. Full-scale T-39 in test section of 80 ft × 120 ft facility of the NFAC (photo courtesy of the NASA Ames Research Center).



Fig. 46. Full model of A3XX during ground effect testing in DNW-LLF (photo courtesy of DNW).

Fig. 48. Trapezoidal wing model with full-span slat and flap mounted in the 12 ft PWT (photo courtesy of NASA).
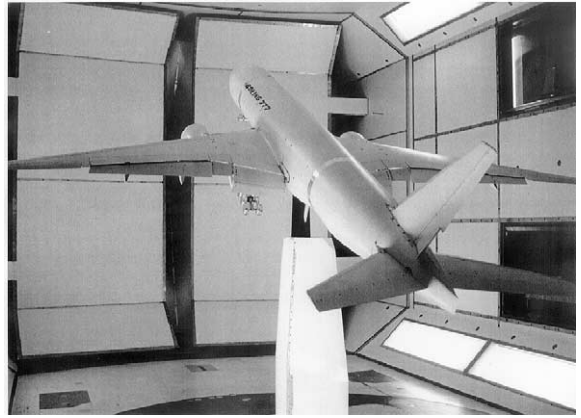


Fig. 49. Full model of B777-200 in DERA 5 m tunnel (photo courtesy of the Boeing Company).



Fig. 50. Full model of A340-600 in test section of ONERA F1 facility (photo courtesy of ONERA).

of 8.7 m (28.5 ft). It has a contraction ratio of 21:1 and contains several coarse- and fine-mesh screens in the settling chamber to further reduce the turbulence level in the test section. The facility was recently renovated and Fig. 48 shows the semispan trapezoidal wing model tested after this renovation [113]. For semispan testing, a splitter plate is installed in the test section. The plate is 5.8 m (19 ft) long and approximately 2.6 m (8.5 ft) wide. The upper surface of the plate is 0.5 m (1.7 ft) above the test section floor, which reduces the effective height of the test section to 2.9 m (9.6 ft).

The DERA 5 m pressure tunnel at Farnborough has been used by Boeing as its primary high-lift testing facility since the NASA Ames 12-ft tunnel was closed for renovation in 1990 [29]. The 5 m tunnel operates at stagnation pressures from 1 to 3 atm. It is capable of a maximum unit Reynolds number of $17.6 \times 10^6 \, \text{m}^{-1}$ $(5.4 \times 10^6 \, \text{ft}^{-1})$ at a Mach number of 0.26 and a maximum Mach number of 0.33 at a unit Reynolds number of $13.4 \times 10^6 \, \text{m}^{-1}$ $(4.1 \times 10^6 \, \text{ft}^{-1})$. This trans- lates into a typical reference chord Reynolds number of approximately $7 \times 10^6$ for a commercial aircraft such as a 6.3%-scale full model of the B777 at a Mach number of 0.26 [29]. Fig. 49 depicts a model of the B777-200 in the high-lift configuration mounted in the DERA 5 m test section.

The ONERA F1 tunnel is a subsonic pressurized tunnel located in Le Fauga-Mauzac, just south of Toulouse. It has a rectangular test section with a width of 4.5 m (14.8 ft), a height of 3.5 m (11.5 ft), and a length of 11 m (36.1 ft). The stagnation pressure can be varied between 1 and 3.85 atm with a maximum unit Reynolds number of $20 \times 10^6 \, \text{m}^{-1}$ $(6.1 \times 10^6 \, \text{ft}^{-1})$ at a Mach number of 0.23 and a maximum Mach number of 0.36 at a unit Reynolds number of $12.3 \times 10^6 \, \text{m}^{-1}$ $(3.8 \times 10^6 \, \text{ft}^{-1})$ as depicted in Fig. 43. For a full model with a span of 3 m (9 ft) at a Mach number of 0.2 this translates into a Reynolds number of $6 \times 10^6$ [4]. Fig. 50 shows a model of the A340-600 in the high-lift configuration mounted using a single strut with internal balance in the tunnel.

The National Transonic Facility (NTF) is a closed loop cryogenic pressure tunnel capable of Mach

Table 4
Maximum Reynolds numbers (in millions) achievable in several wind tunnels compared to flight for the B777-200 [107]

|  |  | Landing, $M_\infty = 0.21$ | Takeoff, $M_\infty = 0.26$ |
| --- | --- | --- | --- |
| DERA 5 m | 6.3% full model | 5.95 | 6.85 |
| Ames 12 ft | 4.2% full model | 8.05 | 9.80 |
| NTF | 5.2% semi-span | 32.5 | 49.0 |
| Flight (sea level) | Full scale | 33.9 | 41.5 |
| Flight (15,000 ft) | Full scale | 22.3 | 27.3 |

numbers from 0.2 to 1.2, stagnation pressures from 1 to 8.9 atm, and a maximum unit Reynolds number of $475 \times 10^6 \, \text{ft}^{-1}$ ($145 \times 10^6 \, \text{ft}^{-1}$) at a Mach number of 1.0. It has a square 2.5 m (8.2 ft) test section with a length of 7.6 m (25 ft). The test gas may be dry air or nitrogen. In the nitrogen mode the operational tunnel temperature is 339 K (150°F) to 116 K (−250°F), although colder test conditions are possible under certain conditions. Table 4 presents a comparison of maximum Reynolds numbers obtainable in various facilities and in flight. Even pressurized at 6 atm, a full model in a pressure tunnel such as the Ames 12-ft tunnel reaches only 24% of full-scale flight Reynolds number. Recently, a study was conducted in the NTF to separate the effects of Mach number, Reynolds number, and dynamic pressure on the high-lift performance of configurations with multi-element flap systems and to answer the question how much Reynolds number is enough for high-lift testing [107]. Unfortunately surface contamination caused by frost prevented completion of this study. Fixes to the frost problem are forthcoming and these tests will resume in the near future. Fig. 51 shows the 5.2%-semispan model of the B777-200 that is being used for the high-Reynolds-number high-lift study in the NTF.

A second cryogenic pressure tunnel is the European Transonic Wind tunnel (ETW) located near the Cologne/Bonn airport in Germany. It has a test section with a height of 2.0 m (6.6 ft), a width of 2.4 m (7.9 ft), and a length of 9.0 m (29.5 ft). Its operating range is Mach 0.15–1.35, stagnation pressure from 1.25 to 4.5 atm, temperature from 313 K (104°F) to 110 K (−262°F), and maximum chord Reynolds number of $85 \times 10^6$ at a Mach number of 0.8. At a for high-lift system development more appropriate Mach number of 0.2, the maximum achievable chord Reynolds number is approximately $30 \times 10^6$ for full models or $50 \times 10^6$ for semi-span models.

Full models as well as semi-span models are featured in this section on wind tunnel testing. Although semi-span models allow testing at higher chord Reynolds numbers, the need to acquire data for airplane stability and control analysis and simulator database often dictates the use of full models for wind tunnel testing during the development process of an airplane. Also, semi-span testing requires careful attention to the



Fig. 51. Semispan model of B777-200 mounted in the NTF test section (photo courtesy of the NASA Langley Research Center).

fuselage stand-off height and shape as well as the wall boundary-layer thickness [110,111].

It is worth noting the large number of corrections applied to wind-tunnel data to correct back to free-air conditions. Typically the standard corrections as presented by Barlow et al. [114] work well for tests of models with small blockage ratios at low angles of attack. However, the wall-interference corrections for wind-tunnel measurements involving high-lift configurations can be large and this may increase the uncertainties in the free-air results. In this case CFD may be required to obtain more consistent wind tunnel to free-air corrections [115].

## 8. Flight experimentation

Flight experimentation plays an important role in the aerodynamic design of multi-element high-lift systems. First, it provides the ultimate proof on how well a high-lift system operates as well as the final validation of the design process based on empirical data, computational analysis and wind tunnel testing. Second, the data is

obtained most of the time at the correct Reynolds and
Mach number conditions. Third, it is often easier and
less costly to instrument a full-scale vehicle than a small
model that will be tested in a pressurized and/or
cryogenic wind tunnel. Two recent flight experiments
on subsonic transport aircraft provide a wealth of
information on the aerodynamic characteristics of 3D
multi-element high-lift systems at full-scale conditions
and will be briefly reviewed here.

An A310-300 was flight tested as part of an extensive
European research program (GARTEUR) on high-lift
systems. The purpose of the experiments was to provide
a greater understanding of the differences between wind
tunnel and flight as reported by Greff [116] and Thibert
[117]. Instrumentation including surface pressures,
boundary layer rakes, unsteady pressure transducers
and hot-film sensors was concentrated in the mid-span
region of the starboard wing as shown in Fig. 52. In
Fig. 53 the total lift coefficient measured using a half-
model in the ONERA F1 tunnel is compared against the
flight-measured lift coefficient for the airplane in the
landing configuration. Good agreement is obtained over
the entire angle-of-attack range with the tunnel-mea-
sured lift curve depicting a slightly steeper slope and a
higher ($\Delta C_L \approx 0.1$) maximum lift coefficient. Detailed
measurements were conducted in the tunnel and in flight
to determine the state of the attachment-line boundary
layer on the slat near the mid-span location. In Fig. 54
the hot-film and fast pressure transducer measurements
are shown for the landing configuration with most of the
measurements indicating laminar flow. On the upper
surface the aft portion of the slat is turbulent under the
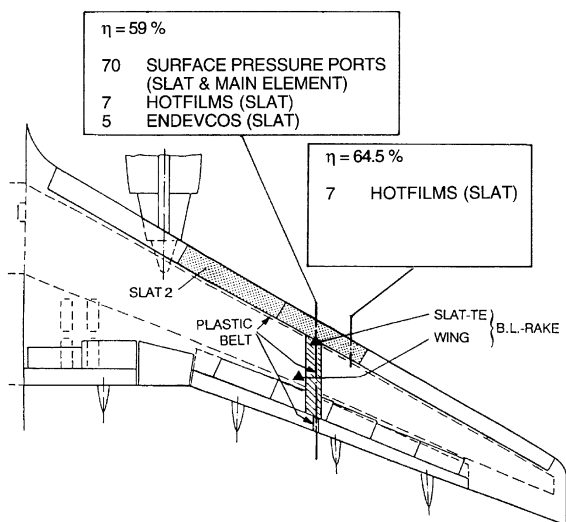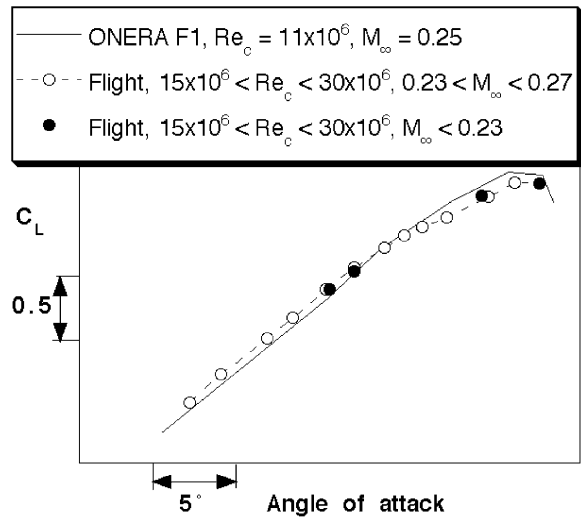influence of the adverse pressure gradient in this region



Fig. 53. Comparison of flight and wind-tunnel measured lift
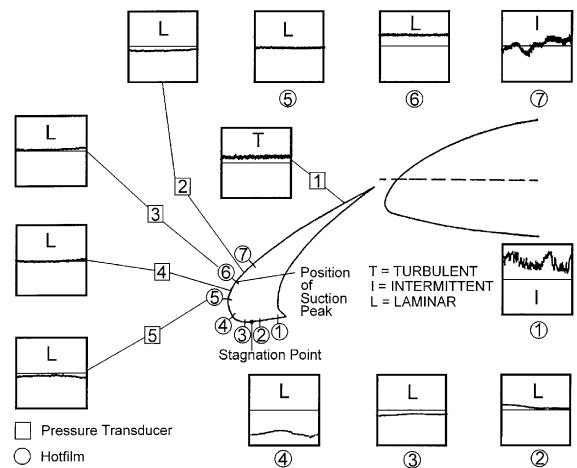curves for the A310-300 in the landing configuration [117].



Fig. 54. Transition detection using hot-film sensors and fast
pressure transducers on A310-300 in landing configuration at
$\alpha = 8.15°$, $M_\infty = 0.24$ [116].

at $\alpha = 8.15°$. This test program led to the following
conclusions:

- The flight and wind tunnel measured lift curves
  agreed well at moderate lift coefficients.
- The flight and wind tunnel measured pressure
  distributions agreed well for the takeoff configura-
  tion. However, some differences were noted on the
  wing upper surface and the flap upper surface for the
  airplane in the landing configuration.
- Both laminar and turbulent attachment line flow was
  observed on the slat.



Fig. 52. Layout of flight test instrumentation on A310-300
[117].

- Laminar flow was detected on the slat at Reynolds numbers well beyond the critical attachment-line Reynolds numbers, $\bar{R} = 245$. This transition Reynolds number was higher than observed in wind tunnel tests.
- Relaminarization was observed on the slat.

A B737-100 (TSRV) was flight tested as part of a multi-phased high-lift research program conducted at the NASA Langley Research Center. The purpose of the program was to document the flow characteristics around a multi-element high-lift system at full-scale flight conditions. Phase I involved surface pressure measurements, skin-friction measurements, and flow visualization on flap elements near the semispan station. Phase II involved surface pressure measurements and flow visualization across the full chord in the same region of the wing [25,26]. Phase III involved not only surface and skin-friction measurements but also boundary-layer profiles, boundary-layer states using hot films, and aeroelastic deformations using an optical system across the full chord near the mid-span station [27,23,24]. Fig. 55 depicts the instrumentation layout used during Phase III of this program and some of the findings were presented and discussed earlier in this paper (Figs. 7 and 8). The B737-100 flight experimentation program resulted in the following conclusions:

- The TSRV with its rear-flight deck digital flight control system provided a very stable flight conditions and allowed achievement of specified conditions with a high degree of accuracy.
- Extended regions of laminar flow were measured on the slat, main element, and fore flap for the airplane in the high-lift configuration.
- Relaminarization was measured on the slat (Fig. 8 at $\alpha > 13°$) and the main element (Fig. 56).



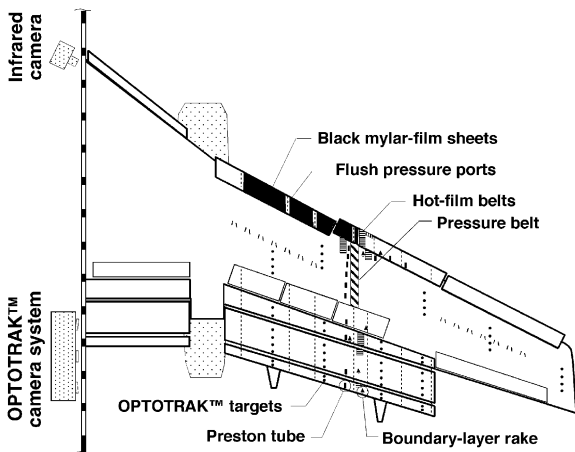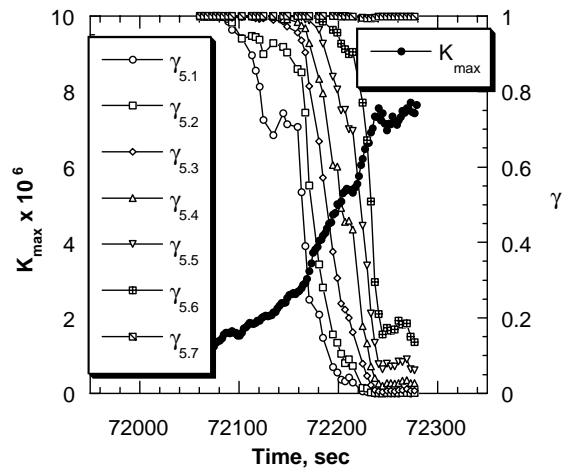Fig. 56. Correlation between hot-film signal intermittency and relaminarization parameter in leading-edge region of main element of B737-100 (TSRV) during slowly decelerating flight in landing configuration [24].

- Slat attachment line was shown to transition at $\bar{R} \approx 350$.
- Transition results from hot-film anemometer system and infrared imaging correlated well.
- Aeroelastic deformations of the flap system were measured using an optical positioning system and shown to be significant.

These A310-300 and B737-100 benchmark flight experiments demonstrate the complexity of the flow physics for multi-element high-lift systems. The fact that extended regions of laminar flow on the high-lift elements are achievable and maintainable (at least for this class of transport airplanes) has significant implications in terms of the requirements that should be put on high-lift model testing in ground-based facilities. If the goal of the test is to accurately predict the high-lift characteristics of the full-scale vehicle in flight, then the extent of laminar flow attained in the model test should match that measured in flight. In addition, these flight results provide insight into what is lacking in the computational tools that are presently used in the design and analysis of high-lift systems.

## 9. High-lift design process

In the previous sections the wide array of computational and physical tools available for the aerodynamic design and analysis of high-lift systems are reviewed. These tools are used at various stages in the design process and the purpose of this section is to provide some insight into this process.

Flaig and Hilbig [4] present a detailed description of the three phases which constitute a high-lift design
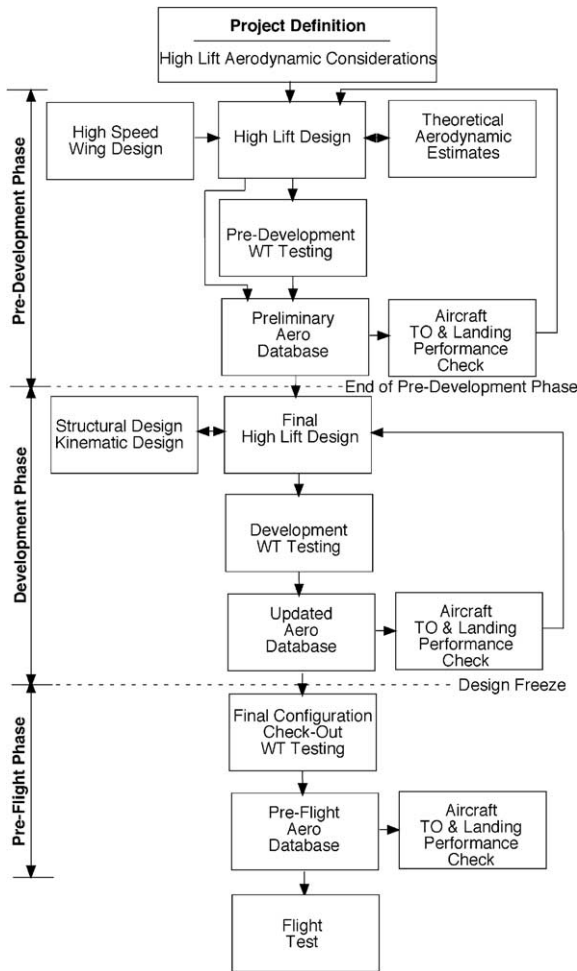


Fig. 55. Layout of flight test instrumentation on B737-100 (TSRV) during phase III of program [27].

Fig. 57. High-lift design process [4].



Fig. 58. High-lift system design considerations [29].

process as depicted in Fig. 57: pre-development, development, and pre-flight. The pre-development process is highly iterative and serves to design and evaluate a wide range of configurations and select the system that best meets the requirements. The design requirements for high-lift systems tend to be extensive as shown in Fig. 58, with inputs from a wide range of groups. Fig. 58 clearly demonstrates that the design of a high-lift system involves much more than just $C_{L_{max}}$ [29]. The pre-development process is computationally intensive but also involves wind tunnel testing to evaluate the aerodynamic performance characteristics of the most promising concepts. Usually at the end of the pre-development phase, a detailed specification and contractual performance guarantees are negotiated with the initial customers for the airplane. This puts great emphasis on the preliminary design methods for estimating high-lift system performance, since takeoff distance, takeoff climb gradients, and landing distance
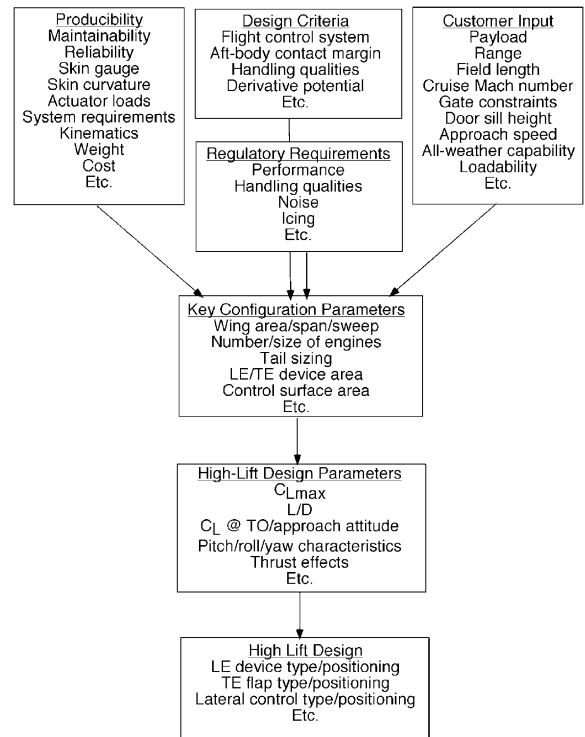
are all critically dependent on the characteristics of the high-lift system. The pre-development wind tunnel testing usually indicates where the major problems are in achieving the performance guarantees. Project approval marks the start of the development phase. In this phase the high-lift configuration that came out of the pre-development phase is refined and transformed into a performance and cost-effective high-lift system that fits within the confines of the final cruise wing design. Wind tunnel testing and extensive interactions with structures and mechanism designers are an integral part of this phase. The transition from development to pre-flight phase occurs with the lines freeze of the configuration. At this point the emphasis shifts to aerodynamic lines and performance validation and the generation of data to support the flight simulator.

Maybe the most striking aspect of this process is the fact that the high-lift designer is not given much design space to come up with an effective system. Both Figs. 57 and 58 show that much of the wing geometry is governed by high-speed design requirements as well as many other considerations. This constrained design space in combination with the many design changes that continuously propagate down the line, and with a competitive commercial airplane market that compresses the available time for design cycles makes high-lift system design very challenging. It may also explain

the diversity of high-lift systems on commercial transport jets as illustrated by Rudolph [1].

## 10. Design examples

In this chapter several design examples for multi-element high-lift systems will be presented. In the first part the focus is on two-dimensional systems whereas in the second part the focus is on three-dimensional systems.

### 10.1. Multi-element airfoils

Eyi et al. [52] present a constrained optimization methodology for multi-element airfoils. The methodology includes the before-mentioned Reynolds-averaged Navier–Stokes method, INS2D, and a commercial gradient-based optimization method. This methodology was applied to optimize the maximum lift coefficient of a three-element airfoil without increasing its drag. The design variables were the gap, overlap, and deflection angle of the slat and the flap. The results of their optimization study are summarized in Table 5. Table 5 shows the changes in lift coefficient and drag coefficient at $8.10°$ and $16.21°$ angles of attack as a result of changes in the design variables. The authors indicate that overlap did not have much effect and, hence, was kept constant. The results show that significant improvements in maximum lift were achieved without penalizing the drag. The computational cost is reported to be modest indicating that these types of design studies are quite affordable on present day computer systems. Greenman et al. [49–51] applied a neural network procedure instead of a gradient-based optimization method to further reduce the computational time required to optimize a multi-element airfoil. Unfortunately these optimization studies were not verified through wind tunnel testing.

As pointed out by R.T. Youngman during a lecture on high-lift devices and their uses by R.R. Duddy, the optimization of the aerodynamic characteristics of multi-element airfoils should not be conducted without taking into account the associated mechanical and structural problems "since an extremely effective wing flap combination might be proposed only to find insuperable difficulties in the way of its practical application" [118]. An early study dealing with this problem is presented by Kuhlman for the DC-7 and DC-8 high-lift systems [119]. Kuhlman [119] points out that the maximum lift coefficient in the landing configuration is typically the determining factor in the selection and design of a high-lift system. However, in the design process serious consideration must be given to the maximum lift coefficient as well as drag coefficient at operating lift conditions for intermediate flap settings. At these intermediate settings, flap gap, overlap, and deflection are determined by the flap support and actuation system. Hence, the extent to which the maximum lift capabilities of a particular flap configuration can be utilized depends significantly on the flap mechanism. Fig. 59 provides some insight into the loss in maximum lift coefficient at intermediate flap settings as a result of the four-bar linkage system used by Douglas on the DC-7 and DC-8.

Recently Mathews [120] conducted a constrained numerical optimization of the aerodynamic characteristics of a two-element airfoil with the flap mechanism providing the constraint. This type of design optimization can provide insight into the mechanism selection and design as demonstrated by the comparison of a track and roller mechanism and a four-bar linkage system as presented by Mathews [120]. A comparison of the flap overlap and gap for a track and roller flap support and actuation system against that of a four-bar linkage system indicates that the latter is capable of generating much larger gaps at small flap angles and, hence, is the preferred system in this situation.

Table 5
Numerical optimization of a three-element airfoil, $Re = 9.0 \times 10^6$, fully turbulent [52]

| Parameter | Initial | Design | Change (%) | Initial | Design | Change (%) |
|---|---|---|---|---|---|---|
| | $\alpha = 8.10°$ | | | $\alpha = 16.21°$ | | |
| | Slat optimization | | | Slat optimization | | |
| $c_l$ | 2.490 | 2.537 | 1.88 | 3.379 | 3.489 | 3.26 |
| $c_d$ | 0.1035 | 0.0950 | −8.24 | 0.1094 | 0.1032 | −5.65 |
| | Flap optimization | | | Flap optimization | | |
| $c_l$ | 2.490 | 2.528 | 1.52 | 3.379 | 3.403 | 0.71 |
| $c_d$ | 0.01035 | 0.01035 | −0.05 | 0.1094 | 0.1086 | −0.75 |
| | Slat and flap optimization | | | Slat and flap optimization | | |
| $c_l$ | 2.490 | 2.561 | 2.84 | 3.379 | 3.515 | 4.02 |
| $c_d$ | 0.1035 | 0.0941 | −9.10 | 0.1094 | 0.0961 | −12.22 |
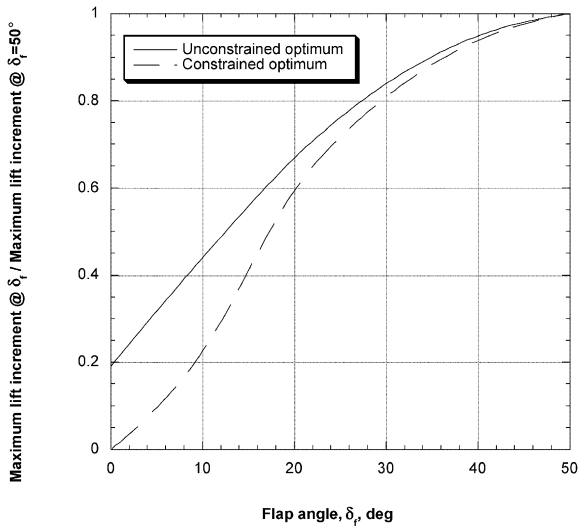
Fig. 59. Effect of mechanism constraint on maximum lift coefficient increment for vane-main flap system [119].



Fig. 60. Effect of flap mechanism on lift coefficient of three-element airfoil at $\alpha = 8°$, $Re = 15.7 \times 10^6$.

Van Dam et al. [121,122] developed a multi-disciplinary approach to quickly and accurately predict the constrained performance characteristics of a trailing-edge flap system. This technique allows a general database of aerodynamic performance to be integrated directly into the mechanism design and analysis. This is accomplished through the application of a commercial software package along with a custom 'loads routine' which incorporates aerodynamic data from CFD. This aerodynamic data is combined with kinematic data of the flap mechanism during deployment. Figs. 60 and 61 present performance results for four typical mechanisms compared with the highest possible performance obtainable at each flap angle. Fig. 60 presents lift performance for the four mechanisms. The discontinuity in the data at 20° is due to the fact that this flap setting was analyzed with the slat in both the landing and takeoff positions. The differences in lift characteristics between the mechanisms are modest, with the largest variation in lift coefficient being approximately 0.15. This is still an appreciable amount considering the earlier examples on the impact small changes can have on typical airliners today. A more interesting result is presented in Fig. 61. This plot presents the $(L/D)_{2D}$ performance of the four mechanisms compared to the maximum attainable performance. Lift-to-drag ratio is an important performance parameter for planes at takeoff where the aerodynamic design is aimed at finding an acceptable compromise between lift capability at takeoff and stall angles of attack and $L/D$ efficiency. For airplanes in the landing configuration, $L/D$ is less important. It may even be possible that the $L/D$ of single-slotted flap high-lift devices may be too good at flap settings used during
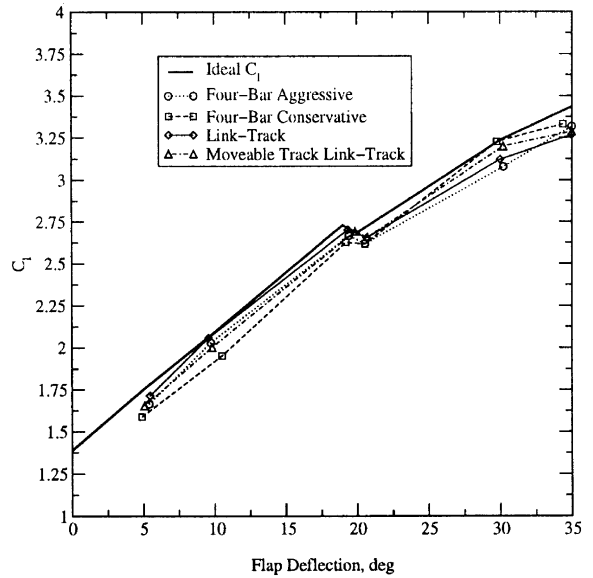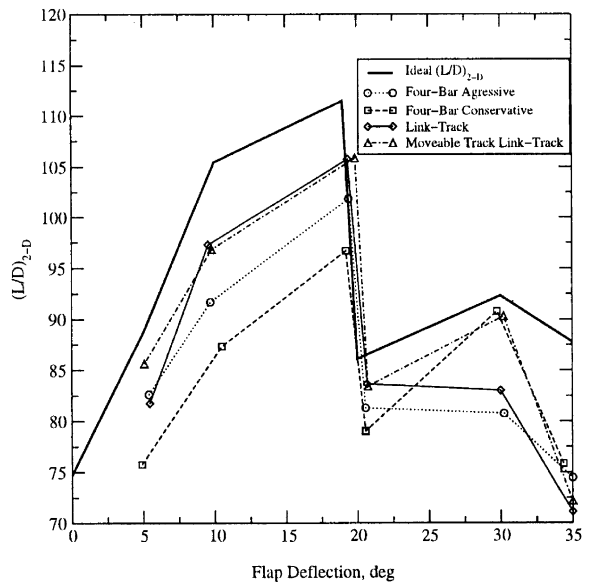


Fig. 61. Effect of flap mechanism on lift-to-drag ratio of three-element airfoil at $\alpha = 8°$, $Re = 15.7 \times 10^6$.

landing, because a certain amount of drag is necessary to maintain a target glide slope. Obviously, the performance of a 2D high-lift configuration differs from that in 3D, but beginning with a good idea of which mechanisms perform well in 2D will shorten the 3D design and analysis process. From Fig. 61, it is clear that no one mechanism is performing close to the optimum $(L/D)_{2D}$ for all flap settings. Especially at the lower flap

angles of 5° and 10° where lift-to-drag ratio is important, these mechanisms leave much to be desired. The best performers at 10°–20° are the two link-track mechanisms with a $\Delta(L/D)_{2D}$ of approximately 8 below optimum at each flap setting. At 5°, the moveable track link-track is the best performer with a $\Delta(L/D)_{2D}$ of approximately 5 below optimum. It is important to note that the two mechanisms with the best Fowler motion progression show a $\Delta(L/D)_{2D}$ of about 10 higher than the poorest of the four mechanisms considered at the lower flap settings.

The results presented in the preceding figures may be obtained without knowledge of the flap deployment mechanism details. Early on, a designer may look at several candidate mechanism configurations and narrow down the field through this type of performance prediction. For example, if climb-out performance is of concern, from Fig. 61 one may be able to eliminate several mechanisms right away based on their $(L/D)_{2D}$ performance at low flap settings. This kind of information early on in the design process can aid the designer in selecting a mechanism type sooner rather than later. These simple mechanism models also give the designer an idea of the complexity and size of the final mechanism. An important issue to cruise performance is the flap mechanism fairing and its drag penalty. The fairing size for each mechanism may be determined in a relative sense through these simple models by examining the model's vertical dimensions.

## 10.2. Multi-element systems

One of the earliest papers on high-lift design for jet transport airplanes was published by Harvey and Norton [123] in 1965. These airplanes with their high wing loading, sweep angles greater than 25°, and different aerodynamic performance demands for takeoff and landing required a major advance in high-lift design. In the paper the design and development work of the B727 high-lift system is presented including aerodynamics and performance and structural and mechanical design. The development relied heavily on wind-tunnel tests but also included an extensive flight experimentation program. The B727 was designed as a short-range transport jet. This resulted in the requirement for relatively high maximum lift coefficient, low approach speed, high ratio of landing to takeoff weight, and good lift-to-drag ratio on takeoff. One compromise made in the design and development process was the incorporation of an inboard high-speed aileron forcing a break in the trailing-edge flaps. Fig. 62 compares the lift curves for the airplane without a high-speed aileron (continuous flap), an outboard high-speed aileron (continuous flap of reduced span), and an inboard high-speed aileron (discontinuous flap). For the B727 with its leading-edge devices the inboard aileron has a small effect on
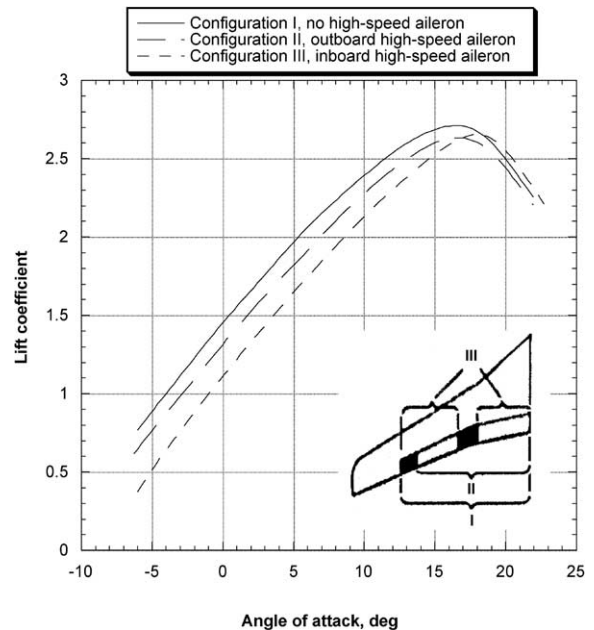


Fig. 62. Effect of high-speed aileron and its placement on the lift characteristics of B727 at 40° flaps as measured in wind tunnel [123].

maximum lift but does reduce lift in the linear range requiring an increase in attitude angle on approach for landing.

The aerodynamic design of the DC-9 wing and its high-lift system are discussed in papers by Shevell and Schaufele [124] and Schaufele and Ebeling [125]. The focus of the former is on the DC-9 Series 10 without leading-edge devices whereas the latter focuses on the Series 20/30/40 with two-position slats at the leading edge. The trailing edge device consists of a continuous double-slotted (fixed-vane/main) flap system. As for the inboard flap design, Schaufele [126] mentions that they went to a three-slot flap arrangement in the area where the main landing gear leg was located in the retracted position as shown in Fig. 63. The flap is continuous to the side of the fuselage, but the two-vane, three-slot configuration was selected to allow the vanes to be compressed to accommodate the main landing gear when retracted. For takeoff a compressed spring arrangement moves the vanes to form a single slotted flap, and for landing, the two vanes are extended to form a triple slotted flap in the inboard area. The leading edge of the upper vane of the triple slotted inboard portion matches the leading edge of the vane in the double slotted outboard portion, so that the flap planform in landing is maintained at 36% of wing chord all the way to the side of the fuselage. This configuration is common to all DC-9s through the Series 50, and is still incorporated on the B717, which structurally and
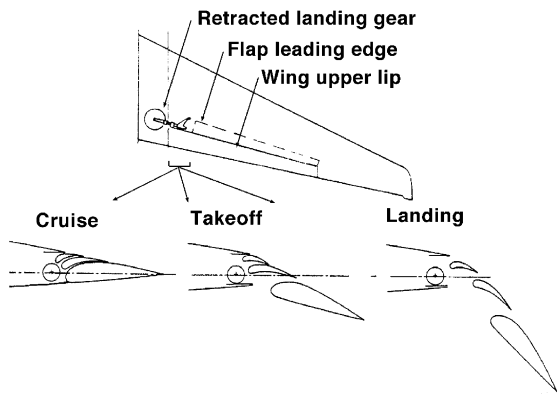
Fig. 63. Double-vane/main flap configuration in wing-root region of DC-9 [125].



Fig. 64. Spanwise lift distribution of B737-300 at 15° flaps [85].

aerodynamically is the DC-9 Series 30. The inboard flap was changed on the MD-80, where a new inboard wing section was added, and the landing gear attachment and retraction scheme were modified. In addition the three-position slat concept from the DC-10 was adopted to replace the two-position slats on the DC-9 [127].

The B737 started out as a small two-engine transport jet designed primarily to operate over short distances from short runways. An important difference between the B727 and B737 high-lift system is that the latter incorporates a three-position slat system instead of the two-position system used on the B727. Olason and Norton [128] present the aerodynamic development of the B737 Series 100/200. The move from turbojets and low-bypass-ratio turbofans to higher-bypass-ratio turbofans and the resulting requirement for a close-coupled nacelle spurred a redesign of the airplane, including its high-lift system. The high-lift design changes for the Series 300/400/500 are discussed and computationally analyzed by Tinoco et al. [85]. The B737 has a relatively high-aspect-ratio wing with a powerful Fowler flap system. This combination has led to significant changes in the spanwise incidence angle distribution and high-lift system performance as a result of aeroelastic wing twist. This wing twist distribution was measured in flight and compared against the jig twist distribution. Using a panel method, Tinoco et al. [85] were able to quantify the aeroelastic twist effect on the spanwise lift distribution as shown in Fig. 64. These results demonstrate that accurate geometry definition in the computation model is needed to obtain good agreement with flight-measured data. Recently, the airplane went through a major redesign resulting in the B737 new generation (NG). In the process, the high-lift system was significantly simplified as outlined by McLean et al. [129].

McRae [130] presents an insightful paper on the aerodynamic design of the cruise and high-lift wing of the A300B. The A300B was designed as a short or
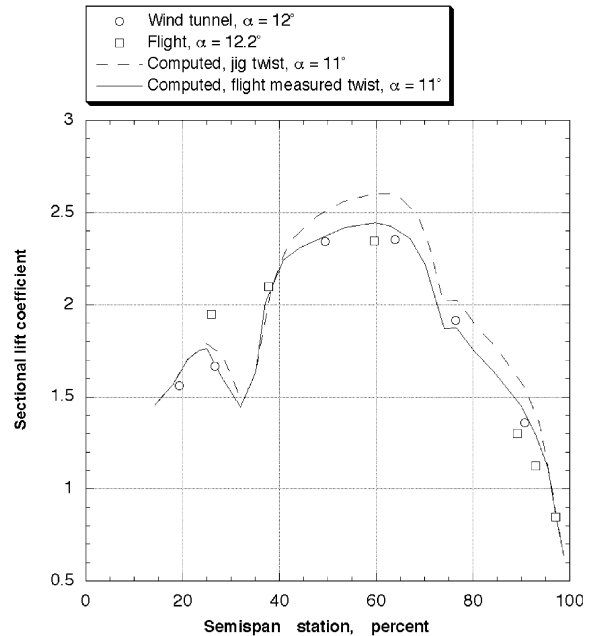
medium range aircraft with a wing aspect ratio of 7.72 and a quarter-chord sweep angle of 28°. The wing is somewhat unique in that it includes a combined spoiler and (inboard) aileron system for roll control and, hence, lacks an outboard aileron. Tabbed Fowler flaps were selected over the triple-slotted flaps used by Boeing at that time. A restraint on mechanical complication was an important factor in this design decision. One of the interesting facts that can be gleaned from this paper is the importance of including details such as slat tracks in the aerodynamic optimization of the high-lift wing. McRae [130] explains that the slat position was originally optimized without the slat tracks in place. Adding the tracks during follow-on wind tunnel tests resulted in a "catastrophic loss of some 80% of slat effectiveness". Re-optimization of the slat with tracks in place resulted in a significantly lower optimum slat position and the resulting lowering of the slat tracks "reduced the track losses to an acceptable level, though it did not quite eliminate them". Fig. 65 shows the slat in the retracted and deployed position and identifies the cut-out necessary to accommodate the slat track and attachment assembly. A door is provided to close the hole in the fixed leading edge.

A discussion on the high-lift system and characteristics of the B747 can be found in papers by McIntosh and Wimpress [131] and Wimpress [132]. The B747 has a wing aspect ratio of 7 (Series 100–300) and a quarter-chord sweep back of 37.5°. The trailing-edge flap system is similar to that used on the B727 and B737 with

Cruise configuration
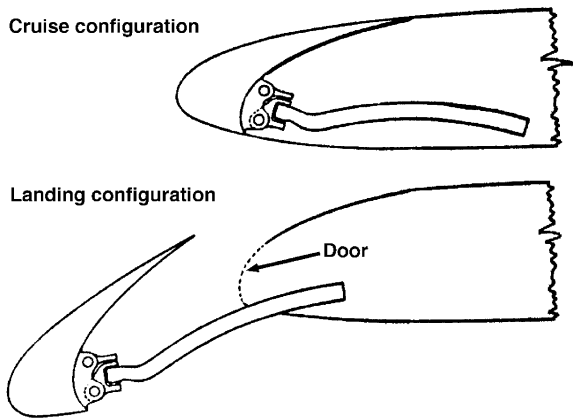
Landing configuration

Door

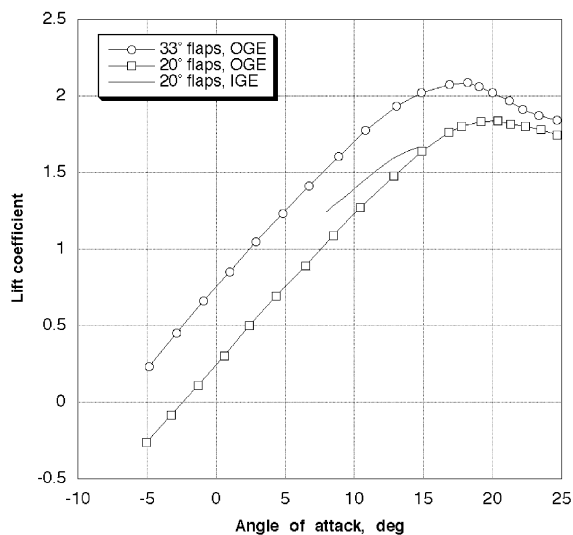Fig. 65. A300B slat and fixed leading-edge arrangement [130].



Fig. 66. High-lift wind-tunnel results for B747 in free air and in ground effect [132].

a high-speed aileron dividing the inboard and outboard elements. The leading-edge system consists of sealed flat-panel bull-nose Krüger flaps inboard and vented variable camber Krüger flaps outboard. An interesting aspect that is discussed is the effect of ground proximity on the high-lift characteristics. Fig. 66 shows the lift results for the airplane in the landing configuration at $33°$ flaps and takeoff at $20°$ flaps as measured in the UWAL tunnel and corrected to unbounded flow conditions. Also shown is the flaps-20 lift curve in ground effect. As brought up by B. Laschka [133] in the discussion following the presentation on the B747 high-lift characteristics by J.K. Wimpress [132], both maximum lift coefficient and lift curve slope are reduced in ground effect. The reply to Laschka's question provides

insight into another important aspect of the aerodynamic design of high-lift systems: "The effect of ground proximity on lift curve slope…in my paper do agree with a theoretical analysis. The change in lift due to ground effect is caused by two components of the potential flow pattern. The image of the trailing vortex causes a decrease in downwash at the lifting line which tends to increase the lift at a fixed geometric angle of attack proportional to $C_L$ to the first power. The image of the bound vortex, on the other hand, decreases the local $q$ felt by the lifting line, thereby reducing the lift at a constant geometric angle of attack. This effect is proportional to $C_L^2$ and therefore, becomes dominant at high-lift coefficients. Our experience has been that the ground proximity effects can be evaluated quite accurately by potential flow theory" [132]. Wimpress [132] also deals with the extrapolation of maximum lift results obtained at low to medium Reynolds numbers ($Re = 1 \times 10^6 - 7.5 \times 10^6$) to full-scale flight conditions ($Re = 30 \times 10^6 - 40 \times 10^6$). For the B747 this procedure worked well with the extrapolated maximum lift coefficients falling within 2 percent of the flight measured values.

The high-lift design and development of the F-28 and Fokker 100 is discussed in several publications including Schuringa [134], de Boer [135], Voogt et al. [136], and Obert [137,5]. Particularly the last paper by Obert [5] provides an insightful overview of 40 years of research and development in high-lift aerodynamics including the use of computational methods during the development of the later models. The Fokker 100 is a twin-jet transport airplane for short to medium range operations and is interesting because of the decision not to incorporate a leading-edge device in the high-lift system. Nevertheless the airplane is capable of generating high maximum lift coefficients as shown in Fig. 67 which depicts the certified maximum lift values based on $V_{S_{min}}$ for all flap settings. The process for these predictions is outlined in Fig. 68. Wind-tunnel results obtained at Reynolds numbers ranging from 1 to 3 million for the full model without horizontal tail are extrapolated to the full-scale flight Reynolds number of approximately 10 million. Next these extrapolated maximum lift values were corrected for the addition of stall control devices and the lift generated by the horizontal tail. Lastly the resulting $V_{S_{1g}}$ values were corrected to $V_{S_{min}}$, the minimum speed in the stall maneuver as defined by the certification rules and requirements.

In the mid-1980s, Wedderspoon [30] published a paper on the design and development of the A320 high-lift system. At this point in time computational aerodynamics methods were starting to be used in the design and analysis of high-lift systems, the 5 m pressure tunnel at Farnborough had become available for high Reynolds number testing, and much experience had been gained on the A300 and A310 aircraft as well as
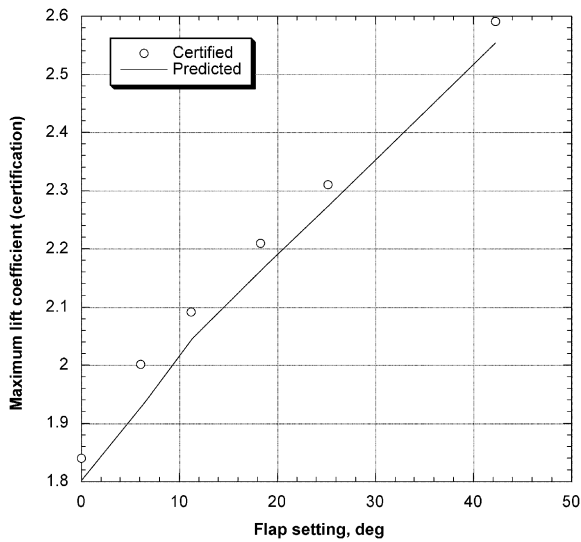
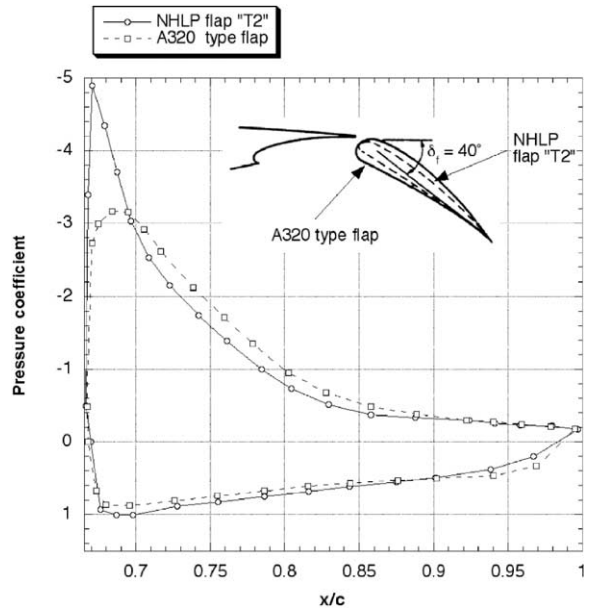Fig. 67. Comparison of predicted and flight-measured maximum lift coefficients for the Fokker 100 [137].



Fig. 69. Effect of larger leading-edge radius on A320 type of flap on pressure distribution at landing setting. Pressures measured in tunnel at $Re = 3.5 \times 10^6$ [30].
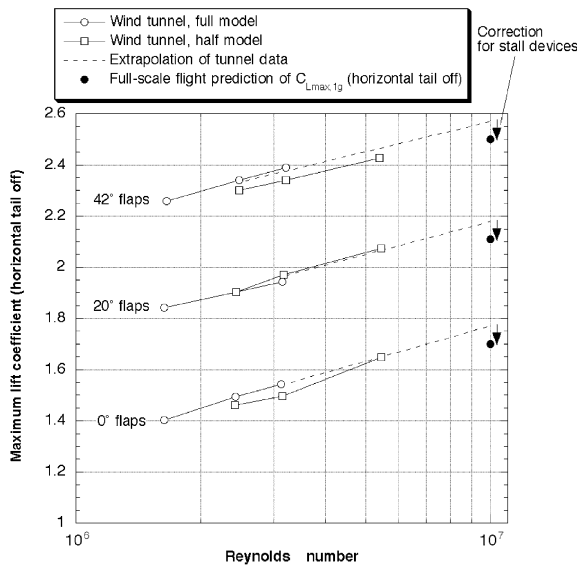


Fig. 68. Prediction of full-scale maximum lift coefficient (horizontal tail off) from wind tunnel result for Fokker 100 [137].

work supported under the UK National High Lift Program [138]. This set the stage for the development of the A320 wing with an aspect ratio of 9.4, 25° of sweep, and nearly full span leading-edge slat and continuous span single-slotted flap. At the leading edge, the designers decided to go for a three-position vented slat instead of a rigid sealed Krüger flap because it had a lower weight, simpler system, and low drag on takeoff

while meeting the maximum lift requirements at landing. At the trailing edge, the fact that the A320 wing section provided sufficient space for a flap with a relatively large leading-edge radius, allowed the designers to select a single-element flap instead of a more complex and heavier double-slotted flap while meeting the maximum lift requirement. Fig. 69 compares the A320 flap and its pressure distribution against an earlier design showing the drop in leading-edge suction peak as a result of the increase in nose radius.

More recent papers by Flaig and Hilbig [4] and Schwetzel [139] give insight into the design and development of the A321 high-lift system. The A321 is a stretched derivative of the A320. This stretching caused a 13 percent increase in the maximum takeoff and landing weight. However, the goal was to retain the cruise as well as takeoff and landing performance of the A320. This forced modifications in the cruise and high-lift wing to account for the growth in weight with major modifications limited to the rear portion of the wing. The outcome of this design and development effort was a slight increase in the chord length along the entire span resulting in a 2.6 percent increase in planform area plus a change from continuous single-slotted flaps to part-span double-slotted (main-aft) flaps. The latter change was dictated by (1) the need to avoid $V_{MU}$ limitations and landing speed increases due to the increase in fuselage length and associated reduction in tail scrape angle and (2) the need to retain the same landing speed
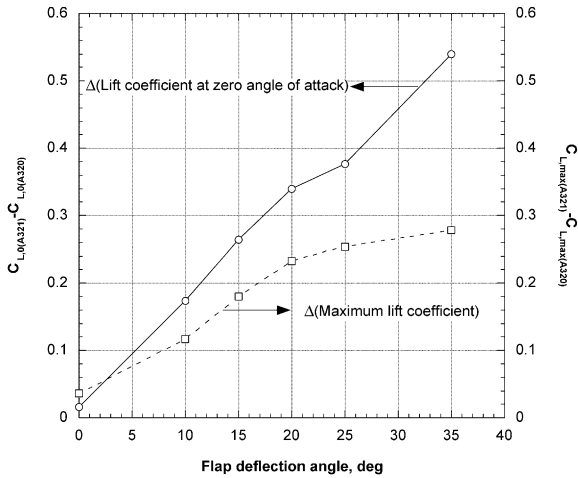
Fig. 70. Comparison of A321 with double-slotted flaps and A320 with single-slotted flaps on high-lift characteristics [4].
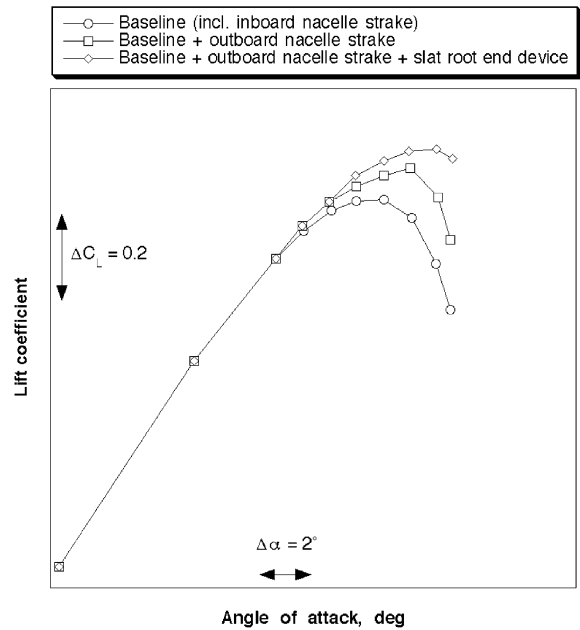


Fig. 71. Effect of slat root end device and outboard nacelle strake on high-lift characteristics of A321 in landing configuration [139].
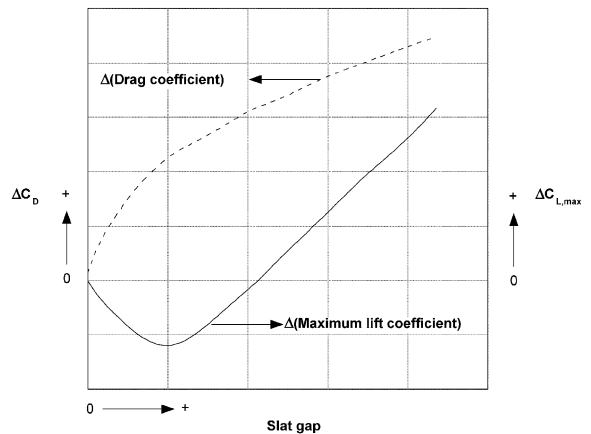


Fig. 72. Effect of slat gap on high-lift aerodynamic characteristics of B777 in takeoff configuration [29].

at a higher weight. This forced an increase in required lift at given angle of attack and an increase in maximum lift coefficient and the addition of a flap element was the only way to generate these changes in lift. The resulting increments in $C_{L_0}$ and $C_{L_{max}}$ as determined during a high-Reynolds-number wind-tunnel test are shown in Fig. 70 and demonstrate the effectiveness of the addition of the partial-span flap. The changes in the fuselage, wing planform and flaps did result in a slight reduction in $L/D$ in the takeoff configuration. Small but important changes in the leading-edge region of the wing made it possible to overcome detrimental aerodynamic effects caused by restricting major design modifications to the rear portion of the wing. Particularly, the addition of a small root device to the inboard slat in combination with an outboard nacelle strake or chine significantly improved the stall characteristics of the high-lift wing and increased maximum lift (Fig. 71).

Nield [29] describes the design process of the B777 high-lift system. The B777 family of airplanes fills the gap between the B767 and B747 as well as replaces the early versions of the B747. The high-lift system was designed using various 2D and 3D computational aerodynamics methods. This computational effort was backed by an extensive wind-tunnel testing program including high Reynolds number entries in the DERA 5 m tunnel at Farnborough. It being a twin-engine configuration, the leading-edge high-lift system consists solely of three-position slats with a sealed position for takeoff and a gapped position for landing as discussed in Section 5. Fig. 72 depicts the effect of slat gap on the maximum lift coefficient and drag for the takeoff setting. The gap is shown to increase drag and to decrease maximum lift for small gaps. The trailing-edge system consists of single-slotted flaps outboard of the nacelle

and double-slotted flaps inboard with a flaperon (high-speed aileron that droops when the flaps are deflected) separating the flaps.

### 10.3. Final observations

Maybe the foremost conclusion that can be drawn from this paper as well as the publications by engineers from leading aircraft manufacturers listed in Section 10.2 is that the design and development of high-lift

systems remains difficult and time consuming. Roger Schaufele was so kind to provide some additional observations regarding the impact of various configuration choices on high-lift design. He was the Project Aerodynamicist on the DC-8, DC-9, and DC-10 and as Vice President of Engineering participated in the development of the MD-11 and C-17. His book on aircraft preliminary design provides more information on the importance of high-lift design for transport jets [140].

Wing-mounted engine nacelles, while very attractive for overall configuration loadability and ease of maintenance, usually involve the use of structural struts or pylons, which have a significant effect on the flow around the wing leading edge, both in cruise and at high-lift conditions. In the early days of jet transports, the pylons that attached the engine nacelles to the wing created enough interference with the flow around the leading edge to limit the effectiveness of the trailing edge flap system in increasing the maximum lift capability of the DC-8 and the B707. In the DC-8 development program, this situation called for much wind tunnel testing with and without the nacelle pylons and extensive data gathering and analysis to understand the flow conditions. It was clear that the installation of the pylons limited the maximum lift coefficient of the configuration and produced a decrement in $C_{L_{max}}$ of about 0.3 (from a pylon-off value of about 2.0 in the landing configuration). This penalty was essentially eliminated by the incorporation of leading edge slots in the final production configuration [141]. These slots only open when the flaps are deployed and are sealed off by flush doors in the cruise configuration. On the B707, the Boeing solution was to add part-span Krüger flaps just inboard of both the inboard and outboard pylons. On the DC-10, the situation was further complicated by the use of leading edge slats. Wind tunnel testing during the development program indicated that again, the nacelle pylons were limiting the maximum lift capability of the configuration with the leading edge slats extended. Many changes to the geometry in the area of the wing leading edge, pylon, and slat intersection were made in order to alleviate the interference. (Fig. 28 is a good example of the complex geometry in this area.) The solution, developed in the wind tunnel and refined during flight testing, was the use of the nacelle strakes or chines that produce a strong vortex flow on the wing upper surface at high-lift conditions and alleviate the adverse effect of the pylon on maximum lift [142].

Another impact of the wing-mounted engine configuration on achievable maximum lift is need to accommodate the jet exhaust that exits in the vicinity of the trailing edge flap for flaps down conditions. Separate inboard and outboard flap segments with a spanwise gap to allow for an inboard aileron and the jet exhaust (e.g., B747) or a flap exhaust gate (e.g., DC-8) have an adverse effect on flap effectiveness, which must be considered in the overall design. On the other side of the configuration picture, designs with aft-mounted engines, while requiring large center of gravity ranges, offer the potential for higher maximum lift capability due to the avoidance of the adverse effects of nacelle pylons at the wing leading edge and jet exhaust cut-outs in the trailing edge flaps. The problems with the aft-engine configurations are of course the need for large center-of-gravity ranges and the susceptibility to the deep stall phenomenon. The requirements for high values of maximum lift coefficient certainly pushed the DC-9 configuration to the aft-mounted engine arrangement as opposed to the B737 wing-mounted arrangement.

Another topic that might be mentioned concerns the interaction between the design of the high-lift system for the high maximum lift capability and the need to obtain satisfactory stalling characteristics (inherent pitch down, mild rolling tendency). This has always been the designer's dilemma. The usual approach for swept wing transports has been to design the wing and high-lift system to obtain an inboard (inboard of 50% $b/2$) initial stall to promote the inherent pitch down and minimize the roll associated with asymmetric outboard stall. This usually starts with the selection or design of the wing airfoils at various spanwise locations, with the airfoils with the highest maximum lift capability being used over the outboard portion of the wing. As noted earlier, on aircraft without leading edge devices and nacelle pylons interfering with the flow around the wing leading edge, the stall is precipitated by the presence of the pylons. In 'treating' the adverse effect of the pylons, less 'treatment' is applied to the inboard pylon area than the outboard pylon area, to ensure that the initial stall occurs at the inboard area, before spreading to the area inboard of the outboard pylon. With the use of full span leading edge devices and inboard trailing edge flaps, the situation becomes somewhat less difficult, since the inboard and outboard segments of the leading edge devices can be 'tailored' to produce the desired values of maximum lift coefficient inboard and outboard. On the DC-10, the leading edge slats for both the takeoff position and the landing position had different deflections for the inboard and outboard segments (more deflection outboard, less deflection inboard) to promote stall progression over the inboard panel. On the DC-9-10 with no leading edge devices, the clean wing leading edge and specially designed high maximum lift airfoils produced an unusually high airplane maximum lift coefficient (about 2.45 in the landing configuration) but the stall was very abrupt and usually asymmetric, which was unacceptable from the characteristics standpoint. The addition of an inboard stall strip and a leading edge fence at about 35% $b/2$ produced an inboard initial stall and adequate stall progression for acceptable stall characteristics, but at the cost of about 0.25 or 10% in

the landing configuration maximum lift coefficient. On the DC-9-20, 30 et al., the initial stall with slats extended was provided by trimming the inboard end of the full-span slat to a slightly more outboard location, another way of 'tailoring' the configuration to produce the highest $C_{L_{max}}$ with acceptable stall characteristics. Boeing did some 'tailoring' on the 727, with the small leading edge fence for the clean stall characteristics, and the combination of the Krüger flaps (relatively lower maximum lift) inboard, and slats (relatively higher maximum lift) outboard. On more recent configurations such as the B737NG and B767-400, small vortillons are installed along the outboard wing leading edge to modify the clean stall characteristics.

## 11. Conclusions

The aerodynamic design of multi-element high-lift systems for transport airplanes has evolved significantly from a largely empirical approach backed by extensive wind-tunnel and in-flight testing in the 1960s to a computational approach backed by limited wind-tunnel and flight tests today. However, the highly competitive and economically driven aviation market of today requires that aircraft manufacturers be able to provide customers with a high-quality product within the shortest amount of time at the lowest possible cost. To further reduce design cycle time and cost, the high-lift design and development process requires further improvements; particularly the computational three-dimensional aerodynamics methods that are being applied. Areas that need attention include:

- Grid generation. Time required to progress from a CAD definition to a volume grid for the CFD analysis of a configuration. Especially for multi-element wings with wing-mounted engine nacelles this step in the aerodynamic design and analysis process is still too time consuming.
- Turbulence modeling in RANS methods. Flows about multi-element high-lift systems are inherently separated and unsteady and wakes play a critical role in the aerodynamic interactions between the various high-lift elements. Most turbulence models in Reynolds-averaged Navier–Stokes methods provide accurate predictions for attached boundary layer flows. However, the predictions tend to become less accurate for separated flows and wakes. Rumsey and Gatski [143] have applied several turbulence models to multi-element airfoil flows and are continuing their efforts to make improvements to these models.
- Boundary-layer transition modeling in RANS methods. For most large jet-propelled transport airplanes with their highly swept wings, laminar flow and

transition are hardly an issue at high speed conditions. At cruise the flow becomes turbulent at or shortly downstream of the leading edge as a result of attachment-line transition or crossflow instability. However, in the high-lift configuration surfaces such as slats and flaps experience much smaller Reynolds numbers and, hence, may support extended regions of laminar flow. This does affect the aerodynamic performance characteristics and, hence, a transition prediction capability is a necessary component of any computational aerodynamics method used in high-lift design.

- Separation bubbles. More than 20 years ago, Dillner et al. [144] commented on the fact that much work remained to be done on the simulation of flows with separation or transition bubbles: "While apparently a mere footnote to the overall high-lift problem, as long as wind tunnel tests continue to be conducted at 'low' Reynolds numbers, the capability to predict the formation and effect of laminar separation bubbles remains an important, imperfectly developed, capability" [144]. Much progress has been made in this area but because these bubbles tend to be small and unsteady, RANS-based maximum lift predictions for flows governed by laminar separation bubbles remain problematic.
- Noting the importance of designing aerodynamically well performing, simpler and less costly high-lift systems, it is critical that high-lift system considerations be included at even the earliest stages of the design process. Presently, few tools are available that facilitate this type of concurrent approach at the conceptual and preliminary design stages.

## References

[1] Rudolph PKC. High-lift systems on commercial subsonic airliners. NASA CR 4746, September 1996.

[2] Meredith P. Viscous phenomena affecting high-lift systems and suggestions for future CFD development. High-Lift System Aerodynamics, AGARD CP 515, September 1993. p. 19-1–19-8.

[3] Ruijgrok GJJ. Elements of airplane performance. Delft: Delft University Press, 1990.

[4] Flaig A, Hilbig R. High-lift design for large civil aircraft. High-Lift System Aerodynamics, AGARD CP 515, September 1993. p. 31-1–31-12.

[5] Obert E. Forty years of high-lift R&D—an aircraft manufacturer's experience. High-Lift System Aerodynamics, AGARD CP 515, September 1993. p. 27-1–27-28.

[6] Abbott IH, von Doenhoff AE, Stivers LS. Summary of airfoil data. NACA TR 824, 1945.

[7] Abbott IH, von Doenhoff AE. Theory of wing sections. New York: McGraw-Hill, 1949.

[8] Cahill JF. Summary of section data on trailing-edge high-lift devices. NACA TR 938, 1949.

[9] Young AD. The aerodynamic characteristics of flaps. ARC R&M 2622, 1953.

[10] Smith AMO. Aerodynamics of high-lift airfoil systems. Fluid Dynamics of Aircraft Stalling, AGARD CP 102, November 1972. p. 10-1–10-27.

[11] Smith AMO. High-lift aerodynamics. J Aircraft 1975;12(6):501–30.

[12] Haines AB. Scale effects on aircraft and weapon aerodynamics. AGARD AG 323, July 1994.

[13] Woodward DS, Hardy BC, Ashill PR. Some types of scale effect in low-speed high-lift flows. ICAS Paper 4.9.3, August 1988.

[14] Gaster M. On the flow along swept leading edges. Aeronaut Q 1967;18:165–84.

[15] Pfenninger W. Laminar flow control laminarization, USAF and NAVY sponsored Northrop LFC research between 1949 and 1967. Special Course on Concepts for Drag Reduction, AGARD Report 654, March 1977. p. 3-1–3-75.

[16] Poll DIA. Transition in the infinite-swept attachment-line boundary-layer. Aeronaut Q 1979;30(Part 4):607–29.

[17] Hall P, Malik MR, Poll DIA. On the stability of an infinite swept attachment line boundary layer. Proc R Soc London A 1984;395:229–45.

[18] Launder BE, Jones WP. On the prediction of relaminarization. ARC CP 1036, February 1969.

[19] Narasimha R, Sreenivasan KR. Relaminarization of fluid flows. In: Yih C-S, editor. Advances in applied mechanics., Vol. 19. New York: Academic Press, 1979. p. 221–309.

[20] Beasley JA. Calculation of the laminar boundary layer and prediction of transition on a sheared wing. ARC R&M 3787, October 1976.

[21] Hardy BC. Experimental investigation of attachment-line transition in low-speed high-lift wind-tunnel testing. Proceedings of the Symposium on Fluid Dynamics of Three-Dimensional Turbulent Shear Flows and Transition, AGARD CP 438, 1988. p. 2-1–2-17.

[22] Arnal D, Juillen JC. Leading-edge contamination and relaminarization on a swept wing at incidence. In: Cebeci T, editor. Numerical and physical aspects of aerodynamic flows IV. Berlin: Springer, 1990. p. 391–402.

[23] Van Dam CP, Los SM, Miley S, Roback VE, Yip LP, Bertelrud A, Vijgen PMHW. In-flight boundary-layer measurements on a high-lift system: slat. J Aircraft 1997;34(6):748–56.

[24] Van Dam CP, Los SM, Miley S, Roback VE, Yip LP, Bertelrud A, Vijgen PMHW. In-flight boundary-layer measurements on a high-lift system: main element and flap. J Aircraft 1997;34(6):757–63.

[25] Yip LP, Vijgen PMHW, Hardin JD, van Dam CP. In-flight pressure distributions and skin-friction measurements on a subsonic transport high-lift wing section. High-Lift System Aerodynamics, AGARD CP 515, September 1993. p. 21-1–21-19.

[26] Yip LP, Vijgen PMHW, Hardin JD, van Dam CP. In-flight pressure measurements on a subsonic transport high-lift wing section. J Aircraft 1995;32(3):529–38.

[27] Yip LP, van Dam CP, Whitehead JH, Hardin JD, Miley SJ, Potter RC, Bertelrud A, Edge DC, Willard PE. The NASA B737-100 high-lift flight research programme—measurements and computations. Aeronaut J 1995;99:372–86.

[28] Niu MCY. Airframe structural design. Hong Kong: Conmilit Press Ltd., 1988. p. 303–57.

[29] Nield BN. An overview of the Boeing 777 high-lift aerodynamic design. Aeronaut J 1995;99:361–71.

[30] Wedderspoon JR. The high lift development of the A320 aircraft. ICAS Paper 86-2.3.2, 1986.

[31] Moens F, Capbern P. Design and testing of leading edge high-lift devices for laminar flow wing applications. High Lift and Separation Control, Royal Aeronautical Society, March 1995. p. 7-1–7-13.

[32] Brune GW, McMasters JH. Computational aerodynamics applied to high-lift systems. In: Henne PA, editor. Applied computational aerodynamics, progress in aeronautics and astronautics., Vol. 125. New York: AIAA, 1989. p. 389–433.

[33] Foster DN, Irwin HPAH, Williams BR. The two-dimensional flow around a slotted flap. RAE R&M 3681, September 1970.

[34] King DA, Williams BR. Developments in computational methods for high-lift aerodynamics. Aeronaut J 1988;92(917):265–88.

[35] Kusunose K, Wigton L, Meredith P. A rapidly converging viscous/inviscid coupling code for multielement airfoil configurations. AIAA Paper 91-0177, 1991.

[36] Drela M. Newton solution of coupled viscous/inviscid multielement airfoil flows. AIAA Paper 90-1470, June 1990.

[37] Drela M. Design and optimization method for multi-element airfoils. AIAA Paper 93-0969, February 1993.

[38] Cebeci T, Jau J, Vitiello D. An interactive boundary-layer approach to multielement airfoils at high lift. AIAA Paper 92-0404, January 1992.

[39] Cebeci T. Calculation of multielement airfoils and wings at high lift. High-Lift System Aerodynamics, AGARD CP 515, September 1993. p. 24-1–24-15.

[40] Le Balleur JC, Néron M. A viscous-inviscid solver for high-lift incompressible flows over multi-element airfoils at deep separation conditions. High-Lift System Aerodynamics AGARD CP 515, September 1993. p. 11-1–11-12.

[41] Arnold F, Thiele F. Laplace interaction law for the computation of viscous airfoil flow in low- and high-speed aerodynamics. AIAA J 1994;31(11):2178–85.

[42] Giles MB, Drela M. Two-dimensional transonic aerodynamic design method. AIAA J 1987;25(9):1199–206.

[43] Drela M, Giles M. Viscous-inviscid analysis of transonic and low Reynolds number airfoils. AIAA J 1987;25(10):1347–55.

[44] Thibert JJ, Reneaux J, Moens F, Preist J. ONERA activities on high-lift devices for transport aircraft. High Lift and Separation Control, Royal Aeronautical Society, March 1995. p. 5-1–5-18.

[45] Capbern P. High-lift research: application to the design of the ATR72 flap. High-Lift System Aerodynamics, AGARD CP 515, September 1993. p. 28-1–28-10.

[46] Klausmeyer SM, Lin JC. Comparative results from a CFD challenge over a 2D three-element high-lift airfoil. NASA TM 112858, May 1997.

[47] Rogers SE, Wiltberger NL, Kwak D. Efficient simulation of incompressible viscous flow over multi-element airfoils. High-Lift System Aerodynamics, AGARD CP 515, September 1993. p. 7-1–7-9.

[48] Rogers SE. Progress in high-lift aerodynamic calculations. J Aircraft 1994;31(6):1244–51.

[49] Greenman RM. Two-dimensional high-lift aerodynamic optimization using neural networks. NASA TM 112233, June 1998.

[50] Greenman RM, Roth KR. High-lift optimization design using neural networks on a multi-element airfoil. J Fluids Eng 1999;121:434–40.

[51] Greenman RM, Roth KR. Minimizing computational data requirements for multi-element airfoils using neural networks. J Aircraft 1999;36(5):777–84.

[52] Eyi S, Lee KD, Rogers SE, Kwak D. High-lift design optimization using Navier–Stokes equations. J Aircraft 1996;33(3):499–504.

[53] Shimha E, Egami K, Amano K. Navier Stokes computation of a high lift system using Spalart Allmaras turbulence model. AIAA Paper 94-0162, January 1994.

[54] Nelson TE, Godin P, Zingg DW. Multi-element airfoil computations with one-equation turbulence models. AIAA Paper 95-0357, January 1995.

[55] Fritz W. Calculation of maximum and high lift characteristics of multi element airfoils. High-Lift System Aerodynamics, AGARD CP 515, September 1993. p. 5-1–5-12.

[56] Dafa'Alla AA, Saliveros E. Comparative study of unstructured and structured Navier–Stokes computations for high lift flows. Proceedings of the Fourth World Congress in Applied Fluid Dynamics, Freiburg, Germany, June 1998.

[57] Jasper DW, Agrawal S, Robinson BA. Navier–Stokes calculations on multi-element airfoils using a chimera-based solver. High-Lift System Aerodynamics, AGARD CP 515, September 1993. p. 8-1–8-11.

[58] Czerwiec R, Edwards JR, Rumsey CL, Bertelrud A, Hassan HA. Study of high-lift configurations using k–ζ transition/turbulence model. J Aircraft 2000;37(6):1008–16.

[59] Barth TJ. Numerical aspects of computing viscous high Reynolds number flows on unstructured meshes. AIAA Paper 91-0721, January 1991.

[60] Davis WH, Matus RJ. High lift multiple element airfoil analysis with unstructured grids. AIAA Paper 93-3478, 1993.

[61] Valarezo WO, Mavriplis DJ. Navier–Stokes applications to high-lift airfoil analysis. J Aircraft 1995;32(3):618–24.

[62] Anderson WK, Bonhaus DL. An implicit upwind algorithm for computing turbulent flows on unstructured grids. Comput Fluids 1994;23(1):1–21.

[63] Anderson WK, Bonhaus DL, McGhee RJ, Walker BS. Navier–Stokes computations and experimental comparisons for multielement airfoil configurations. J Aircraft 1995;32(6):1246–53.

[64] Lindblad IAA, de Cock KMJ. CFD prediction of maximum lift of a 2D high lift configuration. AIAA Paper 99-3180, 1999.

[65] Mavriplis DJ. Adaptive mesh generation for viscous flows using Delaunay triangulation. J Comput Phys 1990;90(2):271–91.

[66] Valarezo WO, Chin VD. Method of prediction of wing maximum lift. J Aircraft 1994;34(1):103–9.

[67] Van Dam CP. Recent experience with different methods of drag prediction. Prog Aerosp Sci 1999;35:751–98.

[68] Rogers SE, Roth K, Nash SM, Baker MD, Slotnick JP, Whitlock M, Cao HV. Advances in overset CFD processes applied to subsonic high-lift aircraft. AIAA Paper 2000-4216, August 2000.

[69] Rogers SE, Roth K, Cao HV, Slotnick JP, Whitlock M, Nash SM, Baker MD. Computation of viscous flow for a Boeing 777 Aircraft in landing configuration. AIAA Paper 2000-4221, August 2000 (also; J Aircraft 2001;38(6):1060–8).

[70] Slotnick JP, An MY, Mysko SJ, Yeh DT, Rogers SE, Roth K, Baker MD, Nash SM. Navier–Stokes analysis of a high wing transport high-lift configuration with externally blown flaps. AIAA Paper 2000-4219, August 2000.

[71] Rudnik R, Melber S, Ronzheimer A, Brodersen O. Aspects of 3D RANS simulations for transport aircraft high lift configurations. AIAA Paper 2000-4326, August 2000.

[72] Takallu MA. Reynolds-averaged Navier–Stokes computations of a high-lift transport model with and without semi-span standoff. AIAA Paper 2000-4222, August 2000.

[73] Pirzadeh SZ. Unstructured grid generation for complex 3D high-lift configurations. SAE Paper 1999-01-5557, October 1999.

[74] Mavriplis DJ. Three-dimensional viscous flow analysis for high-lift configurations using a parallel unstructured multigrid solver. SAE Paper 1999-01-5558, October 1999.

[75] Mavriplis DJ, Pirzadeh S. Large-scale parallel unstructured mesh computations for three-dimensional high-lift analysis. J Aircraft 1999;36(6):987–98.

[76] Mavriplis DJ. Directional agglomeration multigrid techniques for high-Reynolds-number viscous flows. AIAA J 1999;37(10):1222–30.

[77] Berkman ME, Khorrami MR, Choudhari M, Sadowski SS. Investigation of high-lift flowfield of an energy efficient transport wing. J Aircraft 2000;37(1):45–52.

[78] Rudnik R, Melber S, Ronzheimer A, Brodersen O. Three-dimensional Navier–Stokes simulations for transport aircraft high lift configurations. J Aircraft 2001; 38(5):895–903.

[79] Rogers SE, Cao HV, Su TY. Grid generation for complex high-lift configurations. AIAA Paper 98-3011, June 1998.

[80] Nash SM, Rogers SE. Numerical study of a trapezoidal wing high-lift configuration. SAE Paper 1999-01-5559, October 1999.

[81] Hess JL, Friedman DM, Clark RW. Calculation of compressible flow about three-dimensional inlets with auxiliary inlets, slats, and vanes by means of a panel method. NASA CR-174975, 1985.

[82] Epton MA, Magnus AE. PAN AIR—a computer program for predicting subsonic or supersonic linear potential flows about arbitrary configurations using a higher order panel method, Vol. 1, Theory Document (Version 3.0). NASA CR 3251, 1990.

[83] Maskew B. Program VSAERO theory document, a computer program for calculating nonlinear aerodynamic characteristics of arbitrary configurations. NASA CR 4023, 1987.

[84] Ashby DL, Dudley MR, Iguchi SK, Browne L, Katz J. Potential flow theory and operation guide for the panel code PMARC. NASA TM-102851, January 1991.

[85] Tinoco EN, Ball DN, Rice FA. PAN AIR analysis of a transport high-lift configuration. J Aircraft 1987; 24(3):181–7.

[86] Dodbele SM. Three dimensional aerodynamic analysis of a high-lift transport configuration. AIAA Paper 93-3536, August 1993.

[87] Edge DC, Perkins JN. Three-dimensional aerodynamic analysis of a subsonic high-lift transport configuration using PMARC. AIAA Paper 95-0039, January 1995.

[88] Loftin LK, von Doenhoff AE. Exploratory investigation at high and low subsonic Mach numbers of two experimental 6-percent-thick airfoils designed to have high maximum lift coefficients. NACA RM L51F06, December 1951.

[89] Lovell DA. A wind-tunnel investigation of the effects of flap span and deflection angle, wing planform and a body on the high-lift performance of a 28° swept wing. ARC CP 1372, 1947.

[90] Jacob K. A fast computing method for the flow over high-lift wings. High-Lift System Aerodynamics, AGARD CP 515, September 1993. p. 23-1–23-12.

[91] Dutt HNV, Jacob K. Viscous subsonic flow computation for wings with flaps for high-lift. J Aircraft 1993;30(1): 141–3.

[92] Arnold F. Numerical flow simulation on high-lift configurations at Daimler-Benz aerospace airbus. High Lift and Separation Control, Royal Aeronautical Society, March 1995. p. 8-1–8-9.

[93] Ramamurthy RS, Dutt HNV, Holla VS, Swamy MS. Analysis of wings with multi-segmented flaps using a non-planar vortex lattice method. Z Flugwiss Weltraum-forsch 1994;18(2):145–51.

[94] Wakayama S, Kroo I. Subsonic wing planform design using multidisciplinary optimization. J Aircraft 1995; 32(4):746–53.

[95] Van Dam CP, Vander Kam JC, Paris JK. Design-oriented high-lift methodology for general aviation and civil transport aircraft. J Aircraft 2001;38(6):1076–84.

[96] Weissinger J. The lift distribution of swept-back wings. NACA TM 1120, 1947 (translation of February 1942 publication).

[97] Campbell GS. A finite-step method for the calculation of span loadings of unusual plan forms. NACA RM L50L13, 1951.

[98] Blackwell JA. A finite-step method for calculation of theoretical load distributions for arbitrary lifting-surface arrangements at subsonic speeds. NASA TN D-5335, July 1969.

[99] Barnes JP. Semi-empirical vortex step method for the lift and induced drag loading of 2D or 3D wings. SAE Paper 975559, October 1997.

[100] Paris JKF. Advancements in the design methodology for multi-element high-lift systems on subsonic civil transport aircraft. MS Thesis, Davis: University of California, 1999.

[101] Voogt N. Personal communication, July 1997.

[102] Feistel TW, Corsiglia VR, Levin DB. Wind-tunnel measurements of wing-canard interference and a comparison with various theories. SAE Paper 810575, 1981.

[103] Brodeur RR, van Dam CP. Transition prediction for a two-dimensional Navier–Stokes solver applied to wind-turbine airfoils. AIAA Paper 2000-0047, January 2000.

[104] Brodeur RR, van Dam CP. Transition prediction for a two-dimensional Reynolds-averaged Navier–Stokes method applied to wind-turbine airfoils. Wind Energy, 2001;4(2):61–75.

[105] Kusunose K, Cao HV. Prediction of transition location for a 2-D Navier–Stokes solver for multi-element airfoil configurations. AIAA Paper 94-2376, 1994.

[106] Fiddes SP, Kirby DA, Woodward DS, Peckham DH. Investigations into the effects of scale and compressibility on lift and drag in the RAE 5 m pressurised low-speed wind tunnel. Aeronaut J 1985;89:93–108.

[107] Payne FM, Wyatt GW, Bogue DR, Stoner RC. High Reynolds number studies of a Boeing 777-200 high lift configuration in the NASA ARC 12′ pressure tunnel and NASA LaRC National Transonic Facility. AIAA Paper 2000-4220, August 2000.

[108] Stainback PC, Owen FK. Dynamic flow quality measurements in the Langley Low-Turbulence Pressure Tunnel. AIAA Paper 84-0621, January 1984.

[109] Lin JC, Dominik CJ. Parametric investigation of a high-lift airfoil at high Reynolds numbers. J Aircraft 1997;34(4):485–91.

[110] Gatlin GM, McGhee RJ. Study of semi-span model testing techniques. AIAA Paper 96-2386, June 1996.

[111] Gatlin GM, McGhee RJ. Experimental investigation of semispan model testing techniques. J Aircraft 1997;34(4):500–5.

[112] Haftmann B, Debbeler FJ, Gielen H. Takeoff drag prediction for Airbus A300-600 and A310 compared with flight test results. J Aircraft 1988;25(12):1088–96.

[113] Johnson PL, Jones KM, Madson MD. Experimental investigation of a simplified 3D high lift configuration in support of CFD validation. AIAA Paper 2000-4217, August 2000.

[114] Barlow JB, Rae WH, Pope A. Low-speed wind tunnel testing, 3rd ed. New York: Wiley, 1999.

[115] Rogers SE, Roth K, Nash SM. CFD validation of high-lift flows with significant wind tunnel effects. AIAA Paper 2000-4218, August 2000.

[116] Greff E. In-flight measurement of static pressures and boundary-layer state with integrated sensors. J Aircraft 1991;28(5):289–99.

[117] Thibert JJ. The GARTEUR high lift research programme. High-Lift System Aerodynamics, AGARD CP-515, September 1993. p. 16-1–16.21.

[118] Duddy RR. High lift devices and their uses. J R Aeronaut Soc 1949;53(465):859–900.

[119] Kuhlman WH. The Douglas double-slotted flap. In: Lachmann GV, editor. Boundary layer and flow control, Vol. 1. Oxford: Pergamon Press, 1961. p. 453–62.

[120] Mathews JR. The aero-mechanical design of a novel Fowler flap mechanism. High-Lift System Aerodynamics, AGARD CP 515, September 1993. p. 29-1–29-9.

[121] Van Dam CP, Shaw SG, Vander Kam JC, Rudolph PKC, Kinney D. Aero-mechanical design of high-lift systems. Aircraft Eng Aerosp Technol 1999;71(5):436–43.

[122] Van Dam CP, Shaw SG, Vander Kam JC, Brodeur RR, Rudolph PKC, Kinney D. Aero-mechanical design methodology for subsonic civil transport high-lift systems. Aerodynamic Design and Optimisation of Flight Vehicles in a Concurrent Multi-Disciplinary Environment, RTO MP 35, June 2000. p. 7-1–7-12.

[123] Harvey ST, Norton DA. Development of the Model 727 airplane high lift system. SAE Paper 650937, 1965.

[124] Shevell RS, Schaufele RD. Aerodynamic design features of the DC-9. J Aircraft 1966;3(6):515–23.

[125] Schaufele RD, Ebeling AW. Aerodynamic design of the DC-9 wing and high-lift system. SAE Paper 670846, October 1967.

[126] Schaufele RD. Personal communication. November 2001.

[127] Schaufele RD. Applied aerodynamics at the Douglas aircraft company—a historical perspective. AIAA Paper 99-018, January 1999.

[128] Olason ML, Norton DA. Aerodynamic design philosophy of the Boeing 737. J Aircraft 1966;3(6):524–8.

[129] McLean JD, Crouch JD, Stoner RC, Sakurai S, Seidel GE, Feifel WM, Rush HM. Study of the application of separation control by unsteady excitation to civil transport aircraft. NASA CR 209338, June 1999.

[130] McRae DM. The aerodynamic development of the wing of the A300B. Aeronaut J 1973;77:367–79.

[131] McIntosh W, Wimpress JK. Prediction and analysis of the low speed stall characteristics of the Boeing 747. Aircraft Stalling and Buffeting, AGARD LS 74, February 1975. p. 3-1–3-21.

[132] Wimpress JK. Predicting the low-speed stall characteristics of the Boeing 747. Fluid Dynamics of Aircraft Stalling, AGARD CP 102, November 1972. p. 21-1–21-9.

[133] Laschka B. Discussion of Paper 21. Fluid Dynamics of Aircraft Stalling, AGARD CP 102, November 1972. p. A-17.

[134] Schuringa T. Aerodynamics of wing stall of the Fokker F28. Fluid Dynamics of Aircraft Stalling, AGARD CP 102, November 1972. p. 20-1–20-5.

[135] De Boer P. Prediction of aerodynamic loadings on the leading-edge slats of the Fokker F 28 airliner. Prediction of Aerodynamic Loading, AGARD CP 204, September 1976. p. 3-1–3-13.

[136] Voogt N, Mol WJA, Stout J, Volkers DF. CFD applications in design and analysis of the Fokker 50 and Fokker 100. Validation of Computational Fluid Dynamics, AGARD CP 437, May 1988. p. 19-1–19-11.

[137] Obert E. The aerodynamic development of the Fokker 100. ICAS Paper 88-1.6.2, October 1988.

[138] Woodward DS, Lean DE. Where is high-lift today?—a review of past UK research programmes. High-Lift System Aerodynamics, AGARD CP 515, September 1993. p. 1-1–1-45.

[139] Schwetzel D. Improvement of maximum lift in flight by optimisation of vortex flow. High Lift and Separation Control, Royal Aeronautical Society, March 1995. p. 4-1–4-10.

[140] Schaufele RD. The elements of aircraft preliminary design. Santa Ana, CA: Aries Publishing, 2000.

[141] Dunn OR. Flight characteristics of the DC-8. SAE Paper 600378, October 1960.

[142] Callaghan JG. Aerodynamic prediction methods for aircraft at low speeds with mechanical high lift devices. Prediction Methods for Aircraft Aerodynamic Characteristics, AGARD LS 67, May 1974. p. 2-1–2-52.

[143] Rumsey CL, Gatski TB. Recent turbulence model advances applied to multielement airfoil computations. J Aircraft 2001;38(5):904–10.

[144] Dillner B, May FW, McMasters JH. Aerodynamic issues in the design of high-lift systems for transport aircraft. Improvement of Aerodynamic Performance through Boundary layer Control and High-Lift Systems, AGARD CP 365, May 1984. p. 9-1–9-22.